Modeling a Coronal Mass Ejection from an Extended Filament Channel. I. Eruption and Early Evolution

Benjamin J. Lynch[1] , Erika Palmerio[1,2,3] , C. Richard DeVore[4] , Maria D. Kazachenko[5,6] , Joel T. Dahlin[4] ,
Jens Pomoell[3] , and Emilia K. J. Kilpua[3]

[1] Space Sciences Laboratory, University of California–Berkeley, Berkeley, CA 94720, USA; blynch@berkeley.edu
[2] CPAESS, University Corporation for Atmospheric Research, Boulder, CO 80301, USA
[3] Department of Physics, University of Helsinki, FI-00014 Helsinki, Finland
[4] Heliophysics Science Division, NASA Goddard Space Flight Center, Greenbelt, MD 20771, USA
[5] Department of Astrophysical and Planetary Sciences, University of Colorado–Boulder, Boulder, CO 80305, USA
[6] National Solar Observatory, University of Colorado–Boulder, Boulder, CO 80303, USA

Abstract

We present observations and modeling of the magnetic field configuration, morphology, and dynamics of a large-scale, high-latitude filament eruption observed by the Solar Dynamics Observatory. We analyze the 2015 July 9–10 filament eruption and the evolution of the resulting coronal mass ejection (CME) through the solar corona. The slow streamer-blowout CME leaves behind an elongated post-eruption arcade above the extended polarity inversion line that is only poorly visible in extreme ultraviolet (EUV) disk observations and does not resemble a typical bright flare-loop system. Magnetohydrodynamic (MHD) simulation results from our data-inspired modeling of this eruption compare favorably with the EUV and white-light coronagraph observations. We estimate the reconnection flux from the simulation's flare-arcade growth and examine the magnetic-field orientation and evolution of the erupting prominence, highlighting the transition from an erupting sheared-arcade filament channel into a streamer-blowout flux-rope CME. Our results represent the first numerical modeling of a global-scale filament eruption where multiple ambiguous and complex observational signatures in EUV and white light can be fully understood and explained with the MHD simulation. In this context, our findings also suggest that the so-called stealth CME classification, as a driver of unexpected or "problem" geomagnetic storms, belongs more to a continuum of observable/nonobservable signatures than to separate or distinct eruption processes.

Unified Astronomy Thesaurus concepts: Quiet sun (1322); Magnetohydrodynamical simulations (1966); Quiescent solar prominence (1321); Solar filament eruptions (1981); Solar magnetic reconnection (1504); Solar extreme ultraviolet emission (1493); Solar coronal mass ejections (310)

Supporting material: animations

1. Introduction

Large-scale filament eruptions that drive coronal mass ejections (CMEs) are some of the most spectacular energetic and dynamic transients in the solar corona. A well-known property of CME source regions is that the magnetic free energy required to power a solar eruption is concentrated above radial magnetic field polarity inversion lines (PILs) in the form of stressed, sheared, and/or twisted magnetic field structures (e.g., see Patsourakos et al. 2020 and references therein). Pevtsov et al. (2012) examined several large-scale filament channels, i.e., long PILs in the underlying photospheric magnetic field distribution with highly sheared coronal magnetic fields, including those without any discernible filament or prominence material, and showed that these types of coronal structures were responsible for slow- to moderate-speed CME events. Typical low-coronal eruption signatures (e.g., filament eruptions in Hα or extreme ultraviolet (EUV) and ultraviolet (UV) flare ribbons and post-eruption arcades, soft X-ray sigmoid-to-arcade transitions, and/or large-scale coronal dimmings), when followed by halo or partial-halo CMEs, can act as a warning for potential geomagnetic storms

from Earth-impacting CMEs anywhere from 2 to 5 days in advance.

The concept of "stealth CMEs" was first introduced by Robbrecht et al. (2009), who used the multispacecraft viewing perspective of the Solar Terrestrial Relations Observatory (STEREO) spacecraft to analyze a classic, slow streamer-blowout eruption observed at the eastern limb in white-light coronagraph observations from STEREO-A (STA) and with a head-on view from STEREO-B (STB). The event had none of the corresponding on-disk signatures that are usually associated with CMEs. The "stealth CME" classification is necessarily somewhat subjective, based as it is on the interpretation of remote-sensing data and its quality and processing methods. Consequently, we suggest that using the adjective stealthy to describe any individual CME event that appears to be missing one or more of the expected on-disk, low-coronal eruption signatures would be a more appropriate nomenclature. From a space-weather perspective, stealth CME impacts are particularly difficult to forecast as potentially geoeffective ICMEs precisely because they lack the usual on-disk eruption signatures (e.g., Nitta & Mulligan 2017). The resulting "problem" geomagnetic storms are often associated with unexpected ICME interactions with Earth's magnetosphere.

Our previous simulation (Lynch et al. 2016b) of the initiation and low-coronal evolution of a slow, streamer-blowout CME based on the Robbrecht et al. (2009) stealth CME event showed

excellent qualitative agreement with the STEREO-A coronagraph observations. The magnetohydrodynamic (MHD) model successfully replicated several features, including the height and morphology of the X-point flare current sheet in the STA/COR1 field of view (STA saw the stealth CME above the eastern limb), the three-part structure of the flux-rope CME in synthetic running-difference images, and the height–time and velocity profiles of the stealth CME propagation through the STA/COR2 field of view ($\sim$15 $R_{\odot}$). Additionally, the simulation's eruptive-flare reconnection gradually released $\sim$10^{30} erg of magnetic energy over $\gtrsim$20 hr and over such a large spatial extent that the estimated energy flux into the post-eruption arcade system was unlikely to cause observable temperature increase or emission enhancement, providing a natural explanation for the lack of "flare-like" low-coronal signatures. On this basis, we argued that the initiation mechanism for stealth CMEs is not fundamentally different from most slow streamer-blowout CMEs: they simply represent the lowest-energy range of the CME distribution.

In this paper, we extend this argument and build upon the Lynch et al. (2016b) simulation results by modeling the 2015 July 9–10 slow streamer-blowout eruption that originated from an extended, high-latitude filament channel that appeared to span most of the solar disk. There are a number of observable on-disk and off-limb low-coronal signatures associated with this eruption, so this event cannot be considered a stealth CME akin to the Robbrecht et al. (2009) case. However, as described below, our event's low-coronal signatures are somewhat ambiguous when taken individually and present a qualitatively weaker indication that a possibly geoeffective, Earth-directed eruption has taken place, especially compared to most flare-associated CMEs from active regions. Our numerical modeling shows that this particular set of low-coronal signatures can be understood as weak or quasi-stealthy manifestations of the expected flare ribbons and post-eruption flare arcade resulting from a CME eruption following the Lynch et al. (2016b) scenario.

The paper is organized as follows. In Section 2 we describe the 2015 July 9–10 CME event and present the timeline of the nonstandard low-coronal signatures of the filament eruption (Section 2.1) and its morphology and evolution in coronagraph observations (Section 2.2). In Section 3 we describe the MHD numerical modeling methodology (Section 3.1), the initial potential-field source-surface configuration derived from the magnetogram synoptic map for Carrington Rotation (CR) 2165 and background solar wind (Section 3.2), and the boundary flows used to energize the model filament-channel configuration (Section 3.3). In Section 4 we present the simulation results, examining the filament-channel magnetic-field structure and its evolution during CME initiation (Section 4.1), the eruption-related dimming signatures and development of the stealthy flare ribbons and post-eruption arcade system (Section 4.2), and the synthetic white-light coronagraph morphology of the slow eruption (Section 4.3), with direct comparisons to the observations. Finally, in Section 5 we summarize and discuss the implications of our results for the observed dynamics of CME eruptions in the solar corona and space-weather forecasting.

2. Overview of the 2015 July 9–10 Eruption

2.1. Solar-disk Observations

The CME that we analyze originated from the quiet Sun in the southern hemisphere in 2015 July. The CME source region was an extended, high-latitude filament channel that spanned the whole Earth-facing disk in longitude. The large-scale, sheared-arcade field above the global PIL is a common feature of extended filament channels on the Sun (Mackay et al. 2010; Pevtsov et al. 2012). The eruption followed the standard scenario of every large prominence eruption, albeit very slowly: the stressed field of an energized filament channel slowly rose and eventually transitioned to runaway expansion that drove reconnection beneath the erupting structure (e.g., Sterling & Moore 2003; Su & van Ballegooijen 2012; Parenti 2014; Su et al. 2015).

Figure 1 shows a still frame of the filament eruption on 2015 July 10 at 01:00 UT, using four different data sets from the Solar Dynamics Observatory (SDO; Pesnell et al. 2012): magnetograph data from the Helioseismic and Magnetic Imager (HMI; Scherrer et al. 2012) and EUV data in the channels at 211, 304, and 171 Å from the Atmospheric Imaging Assembly (AIA; Lemen et al. 2012). The animated version of Figure 1 showcases on-disk observations of the eruption over the course of 33 hr (from 2015 July 9 at 12:00 UT to 2015 July 10 at 21:00 UT). The high-latitude PIL associated with the eruption is visible in Figure 1(a) extending from limb to limb. Magnetogram data show that the region of quiet Sun to the north of the PIL is predominantly of positive polarity, while the southern region (in the vicinity of the polar coronal hole) is predominantly negative. Each of the AIA channels displayed in Figures 1(b)–(d) shows different manifestations of the gradual filament eruption and post-eruptive evolution.

Before eruption onset, filament material can be identified in both the 211 Å and 304 Å channels. This material is seen to activate and slowly rise starting at around 16:00 UT on July 9. A couple of hours later, at about 18:30 UT, 171 Å imagery (Figure 1(d)) reveals a coronal loop opening off limb to the east of the PIL. This is likely the trace of the eastern leg of the extended filament (anchored behind the eastern limb) lifting off from the Sun. The western spine of the filament, on the other hand, begins to be visible in the 304 Å channel (Figure 1(c)) off limb to the southwest of the solar disk starting around 22:00 UT, with its corresponding opening loops also visible in 171 Å data (Figure 1(d)). Clear coronal dimmings (signatures of CME mass leaving the solar corona; see, e.g., Thompson et al. 2000) can be seen to form in 211 Å imagery (Figure 1(b)) around 00:00 UT on July 10 and progressively migrate away from the PIL. Furthermore, an east-to-west on-disk signature reminiscent of flare-ribbon and post-eruption-arcade evolution is noticeable in the 171 Å channel (some features are visible at 304 Å as well), starting at around 04:00 UT and persisting well beyond July 10 at 21:00 UT.

This extremely large-scale, gradual filament eruption does not occur simultaneously along the entire PIL, rather it erupts asymmetrically (Tripathi et al. 2006; Liu et al. 2009; McCauley et al. 2015). The animated version of Figure 1 shows the eruption signatures starting at the eastern limb, progressing across the disk face, and finishing at the west limb without the impulsive, explosive character of strong-field active-region CMEs.
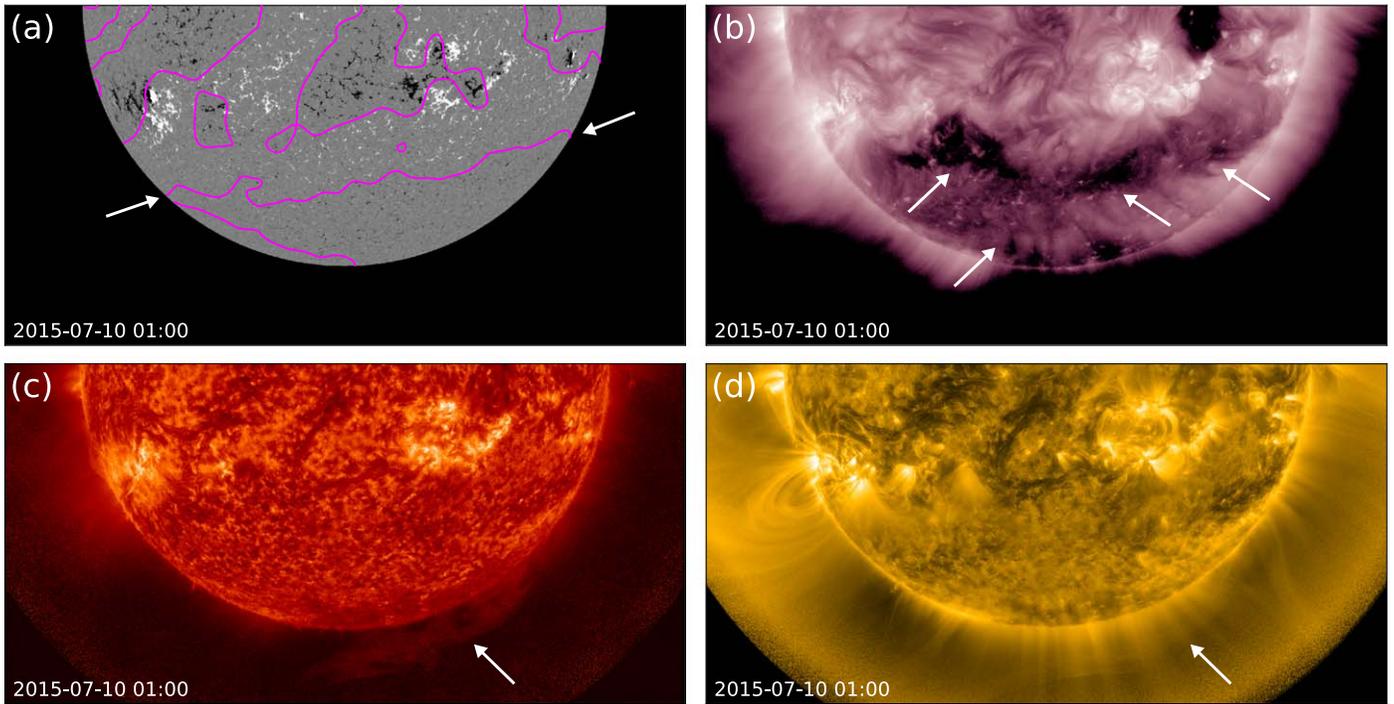
Figure 1. Overview of the 2015 July 9–10 filament eruption in different SDO data sets. (a) HMI line-of-sight (LOS) magnetogram overlaid with the global PILs (in magenta). The PIL involved in the eruption under study is marked with arrows. (b) AIA 211 Å image showing multiple eruption-related coronal dimming areas (marked with arrows). (c) AIA 304 Å image showing the erupting filament material off limb (marked with an arrow). (d) AIA 171 Å image showing opening loops off limb (marked with an arrow). The animated version of this figure runs from 2015 July 9 at 12:00 UT to 2015 July 10 at 21:00 UT and shows the whole eruption process, from the activation of the high-latitude filament to the full development of the post-eruptive signatures.

(An animation of this figure is available.)

2.2. Coronagraph Observations

After its eruption from the Sun, the 2015 July 9–10 CME appeared in coronagraph imagery from the Large Angle Spectroscopic Coronagraph (LASCO; Brueckner et al. 1995) on board the Solar and Heliospheric Observatory (SOHO; Domingo et al. 1995). The east-to-west asymmetry of the eruption at the Sun is well reflected through the solar corona, where the CME proceeded slowly over the course of about one day. Figure 2 shows an overview of the passage of the CME through the C2 and C3 coronagraphs in the LASCO package. The animated version of Figure 2 showcases the evolution of the CME through the solar corona over the course of 32 hr (from 2015 July 9 at 16:00 UT to 2015 July 11 at 00:00 UT).

In the C2 imagery shown in the animated version of Figure 2, the streamer to the southeast of the solar disk swells until the appearance of the leading edge of the CME around 20:00 UT on July 9. This portion of the eruption likely corresponds to the activation of the eastern leg of the filament (described in Section 2.1) and appears in coronagraph data as a slow streamer blowout that is quite narrow (Figures 2(a) and (e)). This ejected material to the southeast of the disk later (at around 03:00 UT on July 10) is followed by the appearance of a more extended, asymmetric feature that sweeps a large part of the southern corona from east to west (Figures 2(b), (c) and (f), (g)). This portion of the eruption likely corresponds to the liftoff of the western filament spine (described in Section 2.1). Finally, at around 14:30 UT on July 10, a structure reminiscent of a three-part CME cavity appears to the southwest of the solar disk and propagates outwards with the western leg of the CME body (Figures 2(d) and (h)). This feature does not appear to have a corresponding counterpart in solar-disk imagery;

nevertheless, the timing and loop-like morphology suggest that it may be associated with the trailing edge of the density-depleted, erupting flux-rope cavity.

In brief, the 2015 July 9–10 CME appeared in coronagraph data as a long-duration (∼24 hr) event that was composed of three portions: a narrow streamer blowout to the southeast; an asymmetric, large ejection throughout the southern hemisphere; and a flux-rope cavity to the southwest.

3. Modeling the Pre-eruption Corona

3.1. Numerical Methods

Our numerical simulation is run with the Adaptively Refined MHD Solver (ARMS; DeVore & Antiochos 2008) code. ARMS solves the 3D nonlinear, time-dependent equations of ideal MHD. It is based on a finite-volume, flux-corrected transport algorithm (DeVore 1991) that advances the equations for the conservation of mass, momentum, and energy, as well as the evolution of the magnetic field and electric currents throughout the system. ARMS utilizes the adaptive-mesh toolkit PARAMESH (MacNeice et al. 2000) to enable efficient multiprocessor parallelization and dynamic, solution-adaptive computational block refinement.

In this simulation, we solve the equations of ideal MHD in an isothermal atmosphere. This formulation does not employ an explicit physical resistivity term in the induction equation, but we note that there are stabilizing numerical-diffusion terms that introduce an effective resistivity at the computational grid scale. The numerical diffusion facilitates magnetic reconnection in regions where current-sheet features and their associated strong gradients have been compressed to the grid scale.
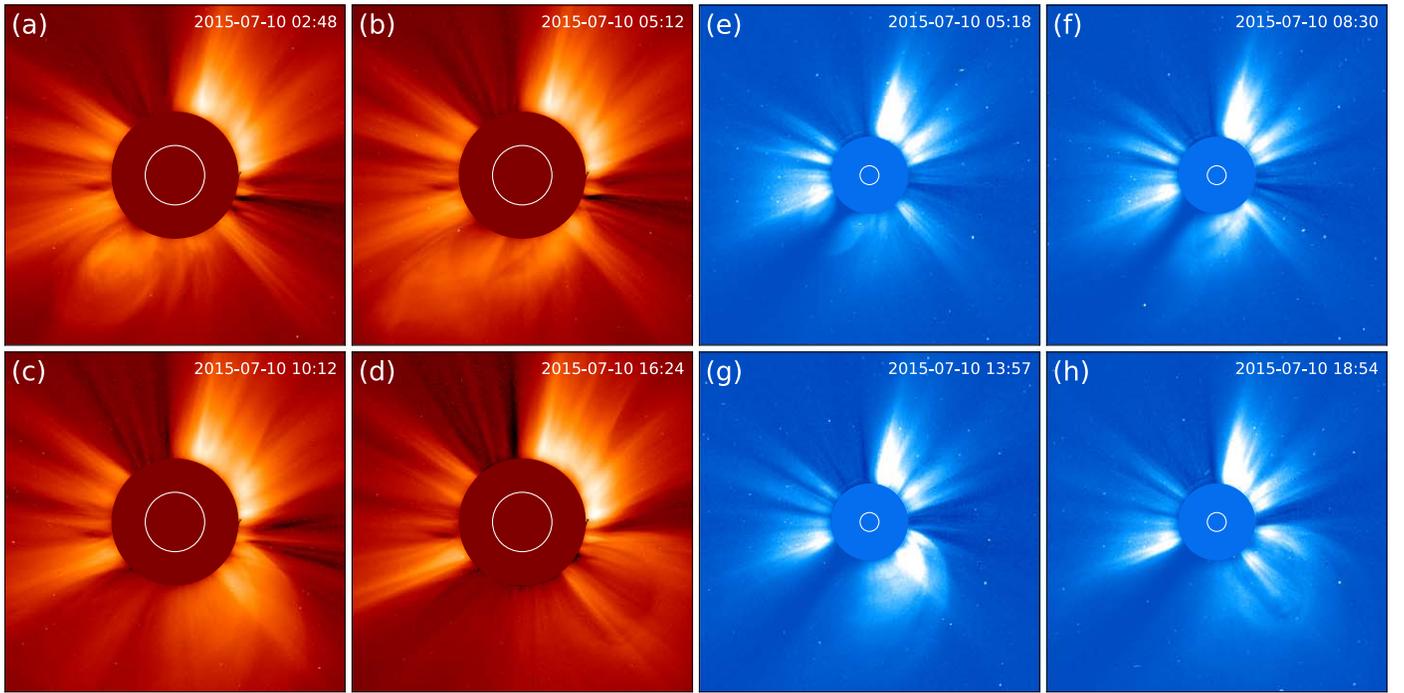
Figure 2. Overview of the 2015 July 9–10 CME eruption as seen in the LASCO coronagraphs. (a)–(d) LASCO/C2 data; (e)–(h) LASCO/C3 data. The animated version of this figure runs from 2015 July 9 at 16:00 UT to 2015 July 11 at 00:00 UT and shows the whole passage of the CME through the fields of view of both coronagraphs.

(An animation of this figure is available.)

The spherical computational domain uses logarithmic grid spacing in r and uniform grid spacing in (θ, ϕ). The domain extends over $r \in [1\,R_\odot, 30\,R_\odot]$, $\theta \in [11°.25, 168°.75]$ ($\pm 78°.75$ in latitude), and $\phi \in [-180°, +180°]$ (longitude). The initial grid consists of $7 \times 7 \times 15$ blocks with 8^3 grid cells per block. Three additional levels of static grid refinement are allowed. The level-3 refinement extends over $r \in [1\,R_\odot, 6.984\,R_\odot]$ for all (θ, ϕ), and a spherical wedge of level-4 refinement centered on the high-latitude filament channel extends over $r \in [1\,R_\odot, 2.642\,R_\odot]$, $\theta \in [82°.65, 168°.75]$, and $\phi \in [0°, 126°]$. This region corresponds to an effective maximum resolution of $448 \times 448 \times 960$. The level-4 grid cells have angular extent $0°.352 \times 0°.375$ in θ, ϕ and radial extent of $\Delta r = 0.00762\,R_\odot$ at the lower boundary.

The boundary conditions are as follows. The ϕ boundary is periodic. The θ boundaries are reflecting for the normal component, and free slip for the tangential components (i.e., zero gradient between the boundary interior cell and the guard cells). On the lower r boundary, the magnetic field is line tied with tangential velocities set to zero. The normal velocity can be positive but not negative, thus allowing the radial guard cells to provide a positive mass flux into the computational domain. The outer r boundary is flow-through (zero gradient) for the normal velocity component and "half-slip" for the tangential components (i.e., the tangential components are set to zero in the guard cells).

3.2. Global Coronal Magnetic Field and Solar Wind

We initialize the simulation magnetic field with the potential-field source-surface (PFSS; e.g., Wang & Sheeley 1992; Luhmann et al. 1998) reconstruction. Figure 3 shows magnetic field observations from the Global Oscillation Network Group (GONG; Harvey et al. 1996) of the National Solar Observatory

(NSO) and two of the derived PFSS visualization data products associated with CR 2165 (top row) and the analogous plots depicting the initial $t = 0$ hr magnetic field configuration of the ARMS simulation (bottom row). Figure 3(a) shows the NSO/GONG zero-point-corrected, daily-updated B_r synoptic map with the high-latitude filament-channel source region indicated by the yellow rectangle; July 9 is indicated by the vertical dashed line at $\phi = +60°$. Figure 3(b) shows the NSO/GONG PFSS reconstruction of the global magnetic geometry including the positive (negative) coronal-hole open-field regions as green (red) areas, the extent of the helmet-streamer belt as the blue field-line projections, and the $B_r = 0$ contour at the 2.5 $R_\odot$ source surface indicating the location of the heliospheric current sheet (HCS) as the black line. Figure 3(c) shows the Earth view of the NSO/GONG PFSS configuration. Figures 3(d), (e), and (f) show the same plots as above but for the simulation's initial magnetic-field configuration, where we have used a truncated harmonic expansion ($\ell_{max} = 25$) in the PFSS calculation. While the active-region-scale features are necessarily underresolved in the ARMS version, the global-scale magnetic geometry is reproduced faithfully. The highest level of grid refinement is centered on the high-latitude filament channel involved in the eruption.

We use the Parker (1958) isothermal solar-wind model to construct the initial outflow conditions of our background solar wind. The number density, pressure, and temperature at the lower radial boundary are given by $\rho_0/m_p = 2.59 \times 10^8$ cm^{-3}, $P_0 = 0.10$ dyn cm^{-2}, and $T_0 = 1.4 \times 10^6$ K, respectively. Hence, the sound speed is $c_0 = 152$ km s^{-1} and the location of the critical point is $r_c = 4.10\,R_\odot$. The solar-wind speed at the outer boundary is $V_{sw}(30R_\odot) = 410$ km s^{-1}. We impose Parker's $V_{sw}(r)$ profile at time $t = 0$ hr and use it to set the
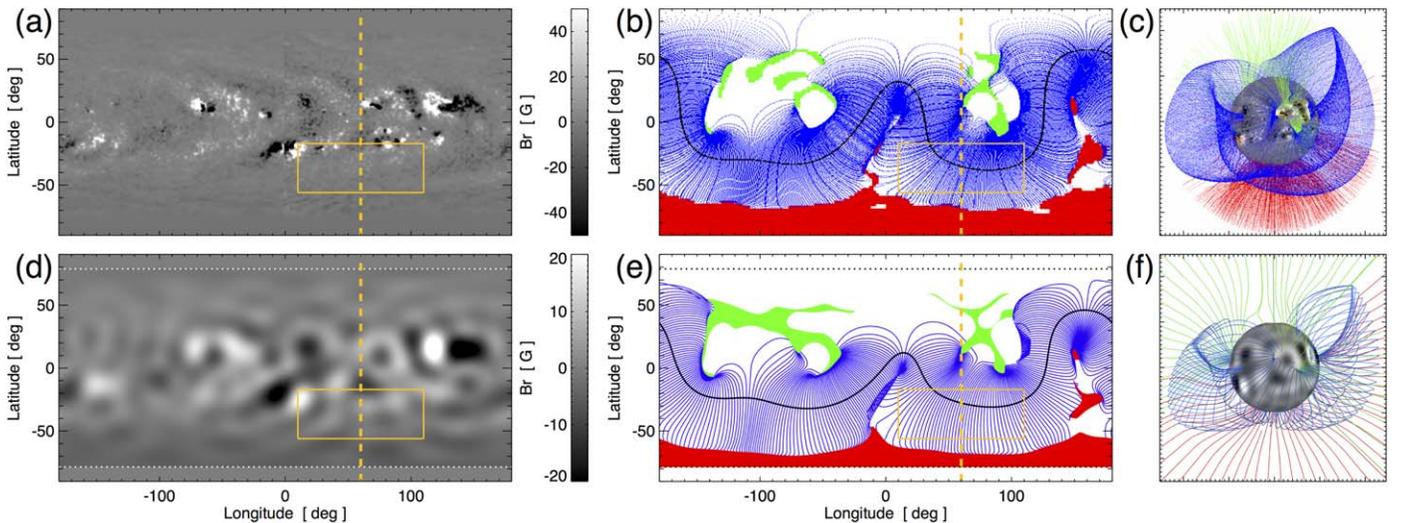
Figure 3. (a) NSO/GONG synoptic map for CR 2165. The day of observation (2015 July 10) is shown as the yellow vertical dashed line and the high-latitude PIL source region for the prominence eruption is the yellow rectangle. (b) NSO/GONG PFSS visualization of coronal-hole regions and helmet-streamer configuration. Green (red) indicates positive (negative) polarity of the radial field, and the black line shows the location of the HCS at the 2.5 $R_\odot$ source surface. (c) NSO/GONG PFSS Earth-view visualization on 2015 July 10. (d) ARMS B_r distribution at the lower boundary. The dashed horizontal lines indicate the latitudinal boundaries of the computational domain. (e) ARMS coronal-hole and helmet-streamer configuration at $t = 0$ hr. (f) Earth-view visualization of the ARMS initial PFSS field structure.

initial mass-density profile $\rho(r)$ from the steady mass-flux condition ($\rho V_{sw} r^2 = $ constant) throughout the computational domain. We then let the system relax until $t = 100$ hr. The solar-wind relaxation process propagates the initial discontinuities in the PFSS solution at the source surface out of the domain and allows the amount of open and closed flux to adjust to the new pressure balance associated with the background outflow. The inner r boundary conditions allow for mass flux into the domain where the density gradients develop, including into the open-field regions, thus providing the solar-wind material.

Our model wind and pre-eruption corona are compared with the white-light coronagraph observations in Figure 4. Figure 4(a) is a composite of the observational pre-eruption data, combining a LASCO/C2 image from 2015 July 9 at 19:00 UT, data from the K-Coronagraph (K-Cor) part of the Coronal Solar Magnetism Observatory (COSMO) taken at Mauna Loa on 2015 July 9 at 18:44 UT, and SDO/AIA 193 Å data from 2015 July 9 at 19:00 UT. Figure 4(b) shows the synthetic white-light brightness ratio image constructed from the ARMS simulation data at $t = 100$ hr. The total brightness ratio $I(t)/I_0$ is calculated from the line-of-sight integration of the Thomson scattering (Billings 1966; Vourlidas & Howard 2006); the intensity I_0 represents the white-light brightness image of the initial, spherically symmetric mass-density profile. Figure 4(c) shows representative magnetic field lines from the same perspective as (b). The open-field lines from each polarity are shown in red and green, and the closed-field streamer-belt field lines are shown in blue. Figure 4(d) shows the same observational data as in Figure 4(a) but including data from the LASCO outer coronagraph C3, in a $30\,R_\odot$ field of view. Figure 4(e) plots an isosurface of $B_r = 0$, visualizing the 3D structure of the HCS, and Figure 4(f) plots the same field lines as Figure 4(c) in the expanded LASCO/C3 field of view. We note that the magnetic-field structure and the highly warped streamer belt in the simulation show quite reasonable qualitative agreement with the coronagraph streamer structures.

3.3. Filament Channel Energization

The eruption originated in the strongly sheared magnetic field of the high-latitude filament channel. This shear, along with the associated magnetic free energy needed to power the CME, is absent from the minimum-energy PFSS configuration. To energize the field and create the filament channel, we employ a statistically averaged version of the helicity condensation model (Antiochos 2013). The Sun is known to generate magnetic helicity in the corona that is predominantly negative (left-handed) in the northern hemisphere and positive (right-handed) in the southern (e.g., Pevtsov et al. 2014), through subtle but persistent mechanisms that remain poorly understood and challenging to observe directly. Both vortical convection at the photosphere and the global-scale distribution of twisted flux emerging into the corona from below may contribute to the hemispheric pattern of injected helicity, which subsequently is transported via magnetic reconnection to PILs of the magnetic field. ARMS simulations have demonstrated that this model forms filament-channel-like coronal structures (Knizhnik et al. 2015, 2017a, 2017b) that, in spherical geometry, can erupt to generate CMEs and associated eruptive flares (Dahlin et al. 2019a). The statistically averaged implementation of the helicity condensation model was developed to support long-duration, full-Sun studies of filament-channel evolution (Mackay et al. 2014, 2018) as well as to facilitate investigations of individual eruptions (Dahlin et al. 2019b, J. T. Dahlin et al. 2021, in preparation) such as the event studied here. This model, in which horizontal magnetic flux is injected directly into the low corona, preferentially adjacent to PILs, is called Statistical Injection of Condensed Helicity (STITCH).

The STITCH sheared-flux generation is calculated from

$$\frac{\partial \boldsymbol{B}_S}{\partial t} = -\frac{1}{\lambda} \boldsymbol{\nabla} \times \left(\sum_{i=1}^{8} \zeta^{(i)} B_r \right) \hat{\boldsymbol{r}} , \qquad (1)$$
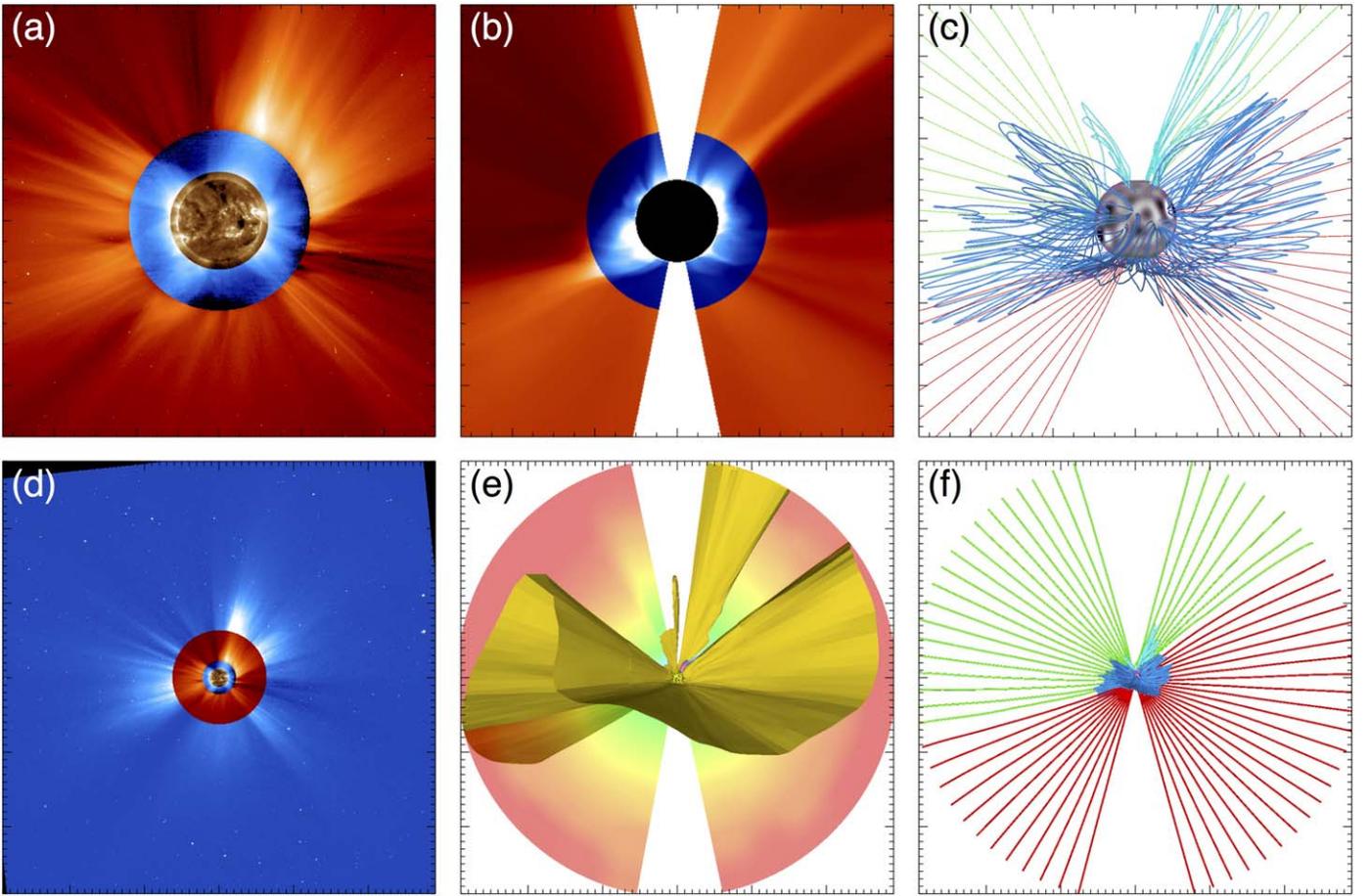
Figure 4. (a) Composite image of the pre-eruption corona using EUV data from SDO/AIA in the 193 Å channel and white-light data from the COSMO/K-Cor and SOHO/LASCO/C2 coronagraphs on July 9 around 19:00 UT. (b) Synthetic white-light intensity ratio image from ARMS simulation at $t = 100$ hr. (c) Representative magnetic field lines showing the helmet-streamer structure of the steady-state solar wind for comparison to pre-eruptive white-light coronagraph structure. (d) Same as (a) with the addition of SOHO/LASCO/C3 data. (e) Visualization of the heliospheric current sheet as the $B_r = 0$ isosurface. (f) Same as (c) for the LASCO/C3 field of view.

where the parameter $\lambda = 5 \times 10^8$ cm is the vertical scale of the helicity injection, $\boldsymbol{B}_S = B_\theta \hat{\boldsymbol{\theta}} + B_\phi \hat{\boldsymbol{\phi}}$, and

$$\zeta^{(i)}(B_r, \theta, \phi, t) = K_0 f_B(B_r) f_\theta(\theta) f_\phi(\phi) f_t(t) \qquad (2)$$

defines a set of spatial and temporal envelope functions with an amplitude coefficient K_0. The envelope functions smoothly ramp the helicity condensation rate to zero outside of the high-latitude filament channel and define the temporal extent of the energization phases used. The mathematical forms of $f_B(B_r)$, $f_\theta(\theta)$, $f_\phi(\phi)$, and $f_t(t)$ are given in Appendix A along with their respective parameter sets. One advantage to this formulation is that the radial-field distribution on the lower boundary remains unchanged throughout the energization: hence, the baseline magnetic energy is fixed during this phase, so that all of the energy added is magnetic free energy available to drive an eruption. The coefficient K_0 has dimensions of diffusivity (length² time⁻¹); its magnitude is determined by the characteristic spatial and temporal scales of the underlying helicity-injecting processes. We refer the reader to Appendix A here for the technical implementation and to the appendix of Mackay et al. (2014) for the derivation of the helicity-injection formalism.

The spatial distribution of the STITCH-injected shear is shown in Figure 5 as the temporal derivatives of the horizontal field components given in Equation (1). The top panel of Figure 5 shows $\partial B_\theta / \partial t$ and the bottom panel $\partial B_\phi / \partial t$, each at the maximum of the temporal envelope function ($f_t = 1.0$) during the energization phase. As can be seen in the figure, we stitched together eight separate patterns of flux injection in our simulation, so that shear was added more or less coherently all along the meandering PIL where the observed eruption occurred.

In this simulation, we employ two distinct energization phases in order to separate clearly the filament channel formation phase, which concentrates the sheared flux along the global PIL, from the activation and eruption phase, which transforms the system from a stable near-equilibrium state to an unstable, runaway eruption. Figure 6 shows the global magnetic and kinetic-energy evolution in our simulation through these two phases. The energization phase lasts from $100 \text{ hr} \leqslant t \leqslant 160$ hr, including 30 hr of STITCH generation of sheared flux with a smooth cosine temporal dependence for $t \in [100, 130]$ hr followed by an additional 30 hr of relaxation to a new equilibrium of the large-scale sheared-flux distribution above the filament channel. Figure 6 plots the change in magnetic energy, $\Delta E_M(t) \equiv E_M(t) - E_M(100 \text{ hr})$, in black and the change in kinetic energy, $\Delta E_K(t) \equiv E_K(t) - E_K(100 \text{ hr})$, in red. The duration of the STITCH driving patterns are indicated with the gray dashed line; the vertical blue dotted line at
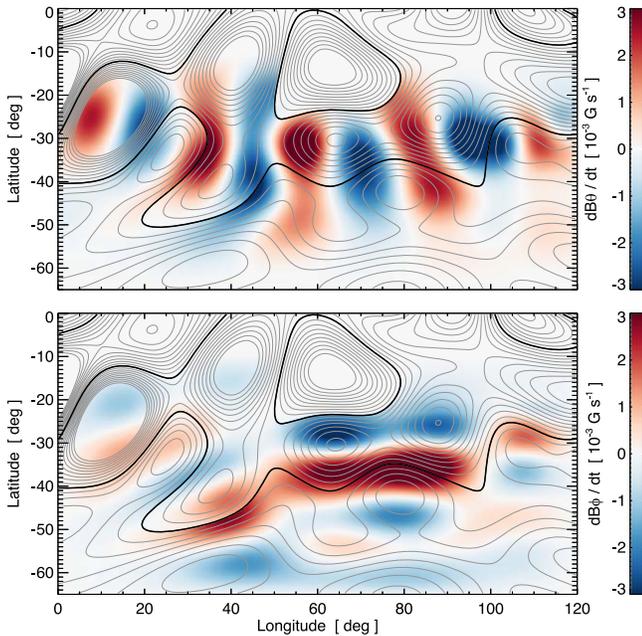
Figure 5. The imposed rates of change $\partial B_\theta / \partial t$ (top) and $\partial B_\phi / \partial t$ (bottom) during the STITCH horizontal-flux injection that energizes the filament channel.
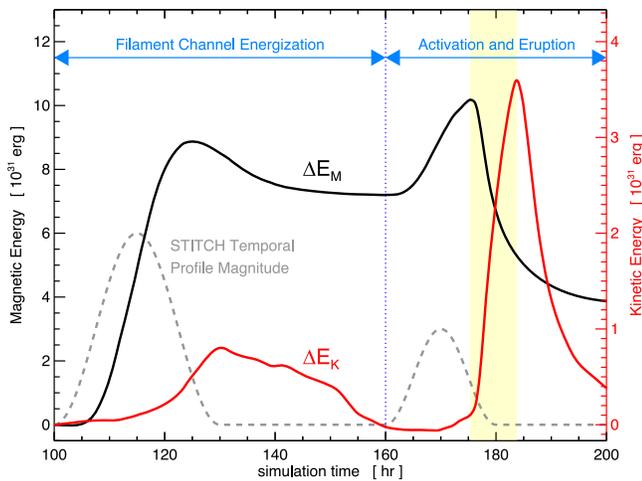

Figure 6. Evolution of the global magnetic (ΔE_M) and kinetic (ΔE_K) energies, together with the temporal profile of STITCH helicity injection, during the two main phases of the simulation: filament-channel energization and activation/eruption. The yellow-shaded region corresponds to the impulsive phase of the eruptive flare.

$t = 160$ hr separates the energization and eruption phases. The total magnetic energy accumulated at the end of the energization phase is $\Delta E_M(160\,\mathrm{hr}) = 7.20 \times 10^{31}$ erg.

Figure 7 shows representative magnetic field lines that illustrate the structure of the sheared filament channel and the overlying flux systems at the end of the energization phase. Figure 7(a) shows the high-latitude filament channel (magenta-to-yellow field lines) on the west limb along with the overlying streamer flux (light blue) and the positive (negative) open fields in green (red). Figures 7(b) and (c) show two close-up perspectives of the sheared filament-channel field lines shown in panel (a). The magenta-to-yellow color scale represents the B_ϕ component: the most sheared field lines with the largest B_ϕ values are magenta, the least sheared are yellow. We note that the field lines develop a weak twist from the structure of the

helicity injection acting on the global PIL. The long horizontal field lines above the PIL form the characteristic dips found in many prominence-field models and observations (e.g., DeVore & Antiochos 2000; Parenti 2014; Gibson 2018; Patsourakos et al. 2020).

4. Modeling the CME Eruption

4.1. CME Initiation and Filament Eruption Dynamics

The evolution of the total magnetic and kinetic energies during the activation and eruption phase, $t > 160$ hr, are shown in Figure 6. Activation is achieved through another period of STITCH energization, this time for a shorter duration (20 hr) and a lower magnitude (50% of the first period) compared to the earlier filament energization phase. The STITCH profiles are depicted by the height of the dashed gray line in Figure 6. During the activation phase, enough additional magnetic energy accumulates to facilitate the transition from stable, slow evolution to an unstable, runaway eruption.

The eruption occurs due to the evolution of the stressed magnetic field and the interaction between the energized filament channel flux and the large-scale, overlying, and adjacent coronal field configurations (e.g., see description in Lynch et al. 2016b). While the STITCH energization does not directly impose a velocity field at the lower boundary, the imposed electric field can be thought of as generating an "effective" footpoint displacement with a velocity v_{eff}. Examining the magnitudes of the velocity field at $r = 1.05 R_\odot$ along the filament channel region, we find $v_{\mathrm{eff}} \leqslant 20\,\mathrm{km\,s^{-1}}$. Because the Alfvén speed, v_A, in the same region ranged from 500–1000 $\mathrm{km\,s^{-1}}$, v_{eff} at the peak of the helicity-injection rate is $\sim$13% of the sound speed and on the order of $\sim$4% of the Alfvén speed, i.e., $v_{\mathrm{eff}}/v_A < v_{\mathrm{eff}}/c_0 \ll 1$. Therefore, our STITCH energization can be considered quasi-static evolution rather than providing any sort of "direct driving" of the eruption.

As in the analysis of our previous CME simulations (e.g., Lynch & Edmondson 2013; Lynch et al. 2019), we define the so-called "impulsive phase" of the eruption as the interval in which a sharp rise in kinetic energy, ΔE_K, coincides with a similarly sharp drop in magnetic energy, ΔE_M. The rapid conversion of magnetic to kinetic energy has been shown to be an excellent indication of the flare current sheet transitioning to fast magnetic reconnection, which is accompanied by the formation and ejection of plasmoids to process the significantly increased transfer of magnetic flux and mass (Karpen et al. 2012; Lynch et al. 2016a, 2019; Dahlin et al. 2019a).

In our simulation, the maximum $\Delta E_M(t_M^*) = 1.02 \times 10^{32}$ erg occurs at $t_M^* = 175.33$ hr and the maximum $\Delta E_K(t_K^*) = 3.60 \times 10^{31}$ erg at $t_K^* = 183.75$ hr. Thus, the impulsive phase corresponds to the time interval $t_M^* \leqslant t \leqslant t_K^*$, shaded yellow in Figure 6. The overall ratio of magnetic-to-kinetic energy conversion during this impulsive phase is

$$\frac{\Delta E_K(t_K^*) - \Delta E_K(t_M^*)}{\Delta E_M(t_M^*) - \Delta E_M(t_K^*)} = \frac{3.494 \times 10^{31}}{4.896 \times 10^{31}} = 71.4\%. \quad (3)$$

Only a small portion of the remaining free magnetic energy released during the impulsive phase is captured in our simulation. There is a modest increase in the total internal energy of 2.58×10^{30} erg (5.3% of the magnetic energy release) associated with adiabatic compression. The remaining 23.3% of the free
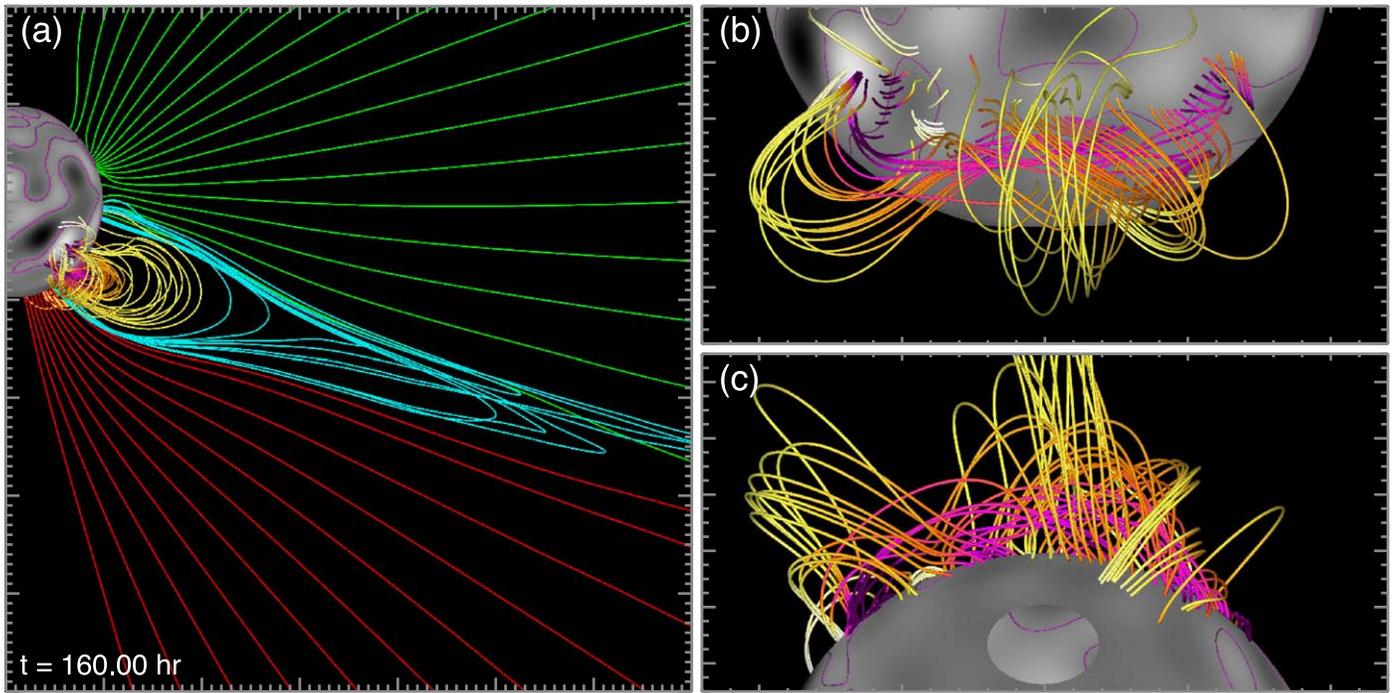
Figure 7. Representative magnetic field lines illustrating the 3D structure of the filament channel. Field lines are colored by flux system at $t = 160$ hr: positive (negative) polarity open fields are green (red), overlying streamer flux is cyan, and filament-channel field lines are colored magenta to yellow, proportional to B_ϕ. (a) Viewpoint from a central meridian of $\phi = -30°$ longitude so that the filament-channel center appears on the limb. (b) Filament-channel field lines from the "Earth view" of $\phi = 60°$. (c) View from above the south pole so that the filament channel appears on the limb, approximately parallel to the plane of the sky. The animated version of this figure runs from $t = 160$ hr to $t = 190$ hr and shows the whole filament-channel activation and eruption process.

(An animation of this figure is available.)

energy released is lost in our isothermal model but would correspond to bulk plasma heating through magnetic and viscous dissipation, enhanced radiation output, and energetic particle acceleration. We note that the total drop in magnetic energy between its maximum at t_M^* and the end of our simulation ($t_f = 200$ hr) is $\Delta E_M(t_M^*) - \Delta E_M(t_f) = 6.31 \times 10^{31}$ erg.

The animation of Figure 7 illustrates the magnetic-field evolution in the low corona during the filament activation ($160\text{ hr} \leqslant t \lesssim 175$ hr) and its eruption resulting in the CME ($t \gtrsim 175$ hr). During the activation phase, the system evolution has two primary features. First, the segment of the helmet-streamer belt above the extended filament channel inflates both laterally and radially. This gradual swelling before an eruption is a common feature of slow streamer blowout CMEs (e.g., Sheeley et al. 1997; Vourlidas & Webb 2018). It can be most easily seen in Figure 7(a) as the overlying streamer cyan field lines and then some of the outermost yellow field lines near the east limb stretching out and "opening up" beyond the edge of the plot window at $r \sim 7R_\odot$ (see also Lynch et al. 2016b). Second, the filament-channel sheared fields rise gradually and asymmetrically, with the eastern limb (left-hand side of panels (b) and (c)) expanding first and the expansion sweeping from east to west along the PIL. The expanding magenta field lines become orange and then yellow with height, indicating the radial falloff of the B_ϕ magnitude. By $t = 176.67$ hr, about half of the filament-channel field lines have opened up and the eruptive-flare reconnection is well underway. The eruption proceeds rapidly thereafter, again sweeping from east to west. By $t = 179.0$ hr, all of the yellow outer filament-channel field lines have opened from the perspective of panels (b) and (c), whereas in panel (a) one sees the CME in the midst of the

eruption having rapidly expanded and acquired a complex, twisted structure that mixes red, green, cyan, and yellow field lines. For $t > 179.0$ hr, the yellow field lines reconnect in the flare current sheet and start to close back down as post-eruption arcade loops. All have reconnected by $t = 184.67$ hr. Plasmoids form in the eruptive-flare current sheet to facilitate the rapid flux transfer and can be seen trailing the eruption (e.g., see frame at $t = 188.67$ hr; also Riley et al. 2007; Webb & Vourlidas 2016; Chae et al. 2017).

It is worth pointing out that the post-eruption filament channel fields do not return to the exact configuration of the pre-energization state. There is still $\Delta E_M(t_f) = 3.87 \times 10^{31}$ erg worth of free magnetic energy stored in the shear and twist in the magnetic fields above the high-latitude PIL after the eruption. This is seen in the ΔE_M energy curve of Figure 6 and is visible at the end of the Figure 7 animation in the lowest-lying field lines. This is essentially a universal feature in both numerical simulations and the observations. The erupting flux does not "open up" all the way to the PIL, rather there remains a comparatively small but nontrivial component of the sheared-field structure of the filament channel.

4.2. Flare Ribbons, EUV Dimmings, and the Post-eruption Arcade

To track the evolution of the reconnection ribbons in the simulation data, we use the Lynch et al. (2019) implementation of the Kazachenko et al. (2017) procedure for analyzing two-ribbon flares in SDO data. The change in field-line length L between successive frames is calculated as $\Delta L = L(t) - L(t - \Delta t)$; we use this as a proxy for the rapid geometric reconfiguration of the magnetic field line connectivity. Our
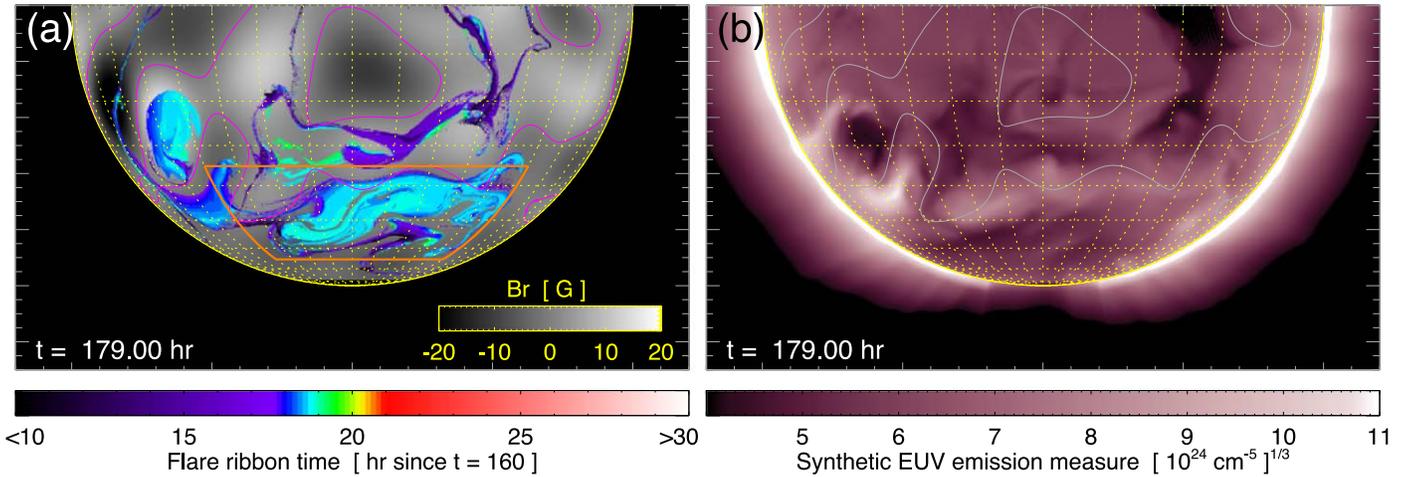
Figure 8. (a) Snapshot at $t = 178.33$ hr of the spatiotemporal evolution of the flare ribbons sweeping out the reconnection flux plotted over the B_r distribution. Magenta lines show the PILs. The orange lines depict the subregion of the reconnection flux used in the calculation of $\Phi_{\mathrm{rxn}}^{\mathrm{ROI}}$ (see text for details). (b) Synthetic EUV emission measure showing the evolution of the coronal dimming regions and the development of the post-eruption arcade. The animated version of this figure runs from $t = 160.33$ hr to $t = 200$ hr and shows the full development of the flare ribbons, dimmings, and post-eruption arcade.

(An animation of this figure is available.)

simulation output frames are in $\Delta t = 20$ minutes intervals, and we track a 768×1568 uniform grid of field lines at the lower radial boundary in (θ, ϕ) over the region $\theta \in [-78^\circ.5, 11^\circ.5]$ and $\phi \in [-30^\circ, 150^\circ]$. If a field line becomes shorter by $\Delta L \leqslant -2R_\odot$ over Δt and both footpoints are connected to the lower $r = R_\odot$ boundary, then we consider that field line (pixel) to have undergone reconnection as either an open-field line closing down or a closed-field line becoming significantly shorter. These reconnection pixels are accumulated in time to create the cumulative ribbon-area map.

Figure 8(a) shows the evolution of the area swept out by reconnection at $t = 178.33$ hr, during the impulsive phase of the eruption, over the B_r distribution at the $r = R_\odot$ boundary from the viewpoint of the SDO observations in Figure 1. The color scale indicates the time when the magnetic flux bundle at a given pixel first reconnects. The large-scale evolution of the ribbon morphology shows qualitative agreement with the generic, universal picture of two-ribbon-flare evolution, in which the ribbons first grow rapidly parallel to the eruption-associated PIL and then expand away from the PIL in the perpendicular direction more slowly (the so-called zipper effect; Moore et al. 2001; Linton & Moldwin 2009; Qiu 2009; Aulanier et al. 2012; Priest & Longcope 2017).

The MHD simulation's large-scale flare-ribbon evolution also shows qualitative agreement with the SDO/AIA observations of the low corona for the 2015 July 9–10 filament eruption. As described in Section 2.1, multiple wavelengths showed an overall east-limb to west-limb evolution of the various eruption signatures on the disk. In Figure 8(a), we see precisely that temporal evolution from east to west in the cumulative ribbon-area map in the impulsive phase.

For a more direct comparison to the SDO/AIA observations, we calculate the time-dependent synthetic EUV emission measure from the simulation's evolving density distribution. The synthetic EUV emission measure is modeled as $I_N(x, y) = \int dz' \, n_e^2(x, y, z')$, where we take $n_e = n_p = \rho/m_p$. We constructed an image from a 512×512 2D array of lines of sight covering the range $-1.2R_\odot \leqslant x \leqslant 1.2R_\odot$, $-1.3R_\odot \leqslant y \leqslant 0.12R_\odot$ and have used 768 samples along the z' direction ($-2R_\odot \leqslant z' \leqslant 2R_\odot$) for the integration of the n_e^2 values. Figure 8(b) shows the resulting

synthetic EUV emission measure at the same time ($t = 178.33$ hr) as the flare-ribbon area map in 8(a). We plot the cube-root of the calculated synthetic EUV intensity, i.e., $(I_N)^{1/3}$, to compensate for the large dynamic range and use the AIA 211 Å color map to facilitate comparison with the corresponding features of Figure 1(b). Here we see both the dynamic formation and evolution of dimmings associated with the flux-rope footpoints and the rapid evacuation of coronal material above the filament channel during the eruption. The latter EUV dimmings are followed by an emission enhancement from the post-eruption arcade (PEA) as the evacuated filament channel refills with coronal material. Here again, we note the east-to-west development of the synthetic EUV features. An animation of this figure is provided in the online version of the article.

The normal magnetic flux swept by the ribbon area on the photosphere corresponds to the flux processed by the flare reconnection in the corona (Forbes & Priest 1983). We calculate the simulation reconnection flux as

$$\Phi_{\mathrm{rxn}}(t) = \frac{1}{2} \int dA [|B_r^{(+)}| + |B_r^{(-)}|], \qquad (4)$$

where $A(t)$ is the cumulative ribbon area shown in Figure 8(a) and $|B_r^{(+)}|$ and $|B_r^{(-)}|$ are the magnitudes of the positive and negative polarities of the radial-field distribution at $r = R_\odot$. Figure 9(a) plots the temporal evolution of Φ_{rxn} (black) and the reconnection rate $d\Phi_{\mathrm{rxn}}/dt$ (blue). The kinetic-energy curve from Figure 6 is shown in gray to illustrate that the onset of fast reconnection occurs prior to the global kinetic-energy rise.

Figure 9(b) plots an estimate of the observed reconnection-flux profile, $\Phi_{\mathrm{rxn}}^{211}$, from the SDO/AIA and HMI data for the 2015 July 9–10 filament eruption. The observational profile uses the sequence of HMI B_{LOS} magnetograms and the PEA area estimate based on the signatures in running-difference 211 Å, i.e., the dimming and refilling of the emission above the PIL. We note that, due to the complexity of AR emission structures north of the high-latitude PIL, our $\Phi_{\mathrm{rxn}}^{211}$ estimate includes only the negative-polarity flux south of the PIL. An equal amount of positive-polarity flux must participate, but it is not unambiguously distinguishable from the AR flux to the north, so we omit it from our calculation. Appendix B describes
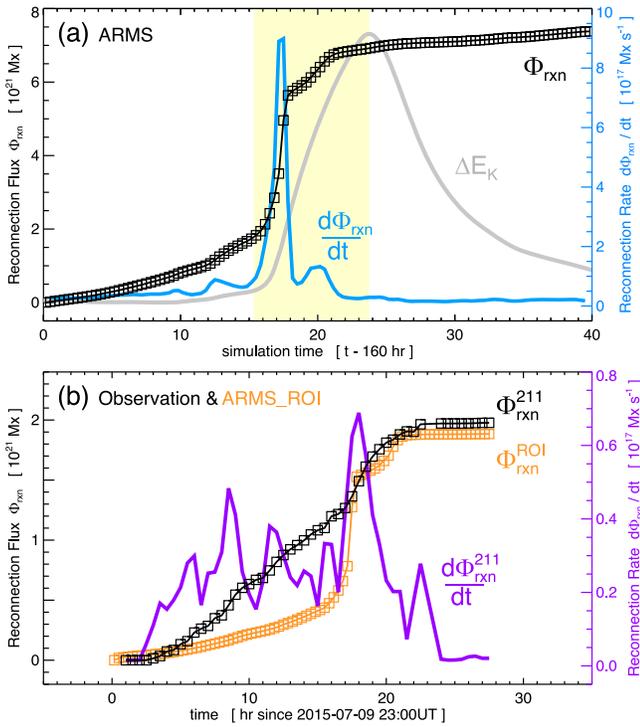
Figure 9. (a) ARMS simulation reconnection flux Φ_{rxn} and reconnection rate $d\Phi_{rxn}/dt$. The yellow-shaded region corresponds to the impulsive phase of the eruptive flare. (b) Reconnection flux and rate (Φ_{rxn}^{211}, $d\Phi_{rxn}^{211}/dt$) estimated from the SDO HMI and running-difference AIA 211 Å observations over the course of the eruption. The Φ_{rxn}^{ROI} reconnection flux is from the ARMS simulation in a $30° \times 90°$ (θ, ϕ) region of interest (ROI) centered on the negative flux side of the filament channel.

the procedure for the observational thresholding used to create the cumulative flare-ribbon maps from the SDO/AIA data.

Figure 9(b) also plots a portion of the total ARMS reconnection flux, Φ_{rxn}^{ROI}, calculated from a region of interest (ROI) defined by $\theta \in [125°, 155°]$ (corresponding to a latitude range of $[-35°, -65°]$) and $\phi \in [20°, 110°]$. Here we use the cumulative ribbon area shown in Figure 8(a) but only with the magnitude of the negative-polarity flux south of the PIL, just as in the observational estimate.

There are both similarities and differences between the model reconnection flux and the observational estimate. For example, the total reconnection flux at the end of the MHD simulation, $t_f = 200$ hr, is $\Phi_{rxn}(t_f) = 7.38 \times 10^{21}$ Mx, whereas the analogous quantity estimated from the AIA observations is $\Phi_{rxn}^{211}(t_{obs,f}) = 1.98 \times 10^{21}$ Mx, where we have taken $t_{obs,f}$ as 2015 July 11 at 03:00 UT. The value of the ROI reconnection flux is almost identical to the observational estimate, $\Phi_{rxn}^{ROI}(t_f) = 1.96 \times 10^{21}$ Mx. The maximum ARMS simulation reconnection rate obtained for both the full pixel map and the ROI portion is $d\Phi_{rxn}/dt = 8.87 \times 10^{17}$ Mx s^{-1}, whereas observationally we estimate $d\Phi_{rxn}^{211}/dt = 6.86 \times 10^{16}$ Mx s^{-1}. The ratio between the simulated and the observational reconnection fluxes is $\Phi_{rxn}/\Phi_{rxn}^{211} \approx 3.7$ with the total reconnection area, but within the ROI area it is $\Phi_{rxn}^{ROI}/\Phi_{rxn}^{211} \approx 0.99$. The reconnection-rate ratio is $(d\Phi_{rxn}/dt)/(d\Phi_{rxn}^{211}/dt) \approx 12.9$ for both the full ribbon area and the ROI area.

The Figure 9(b) comparison between Φ_{rxn}^{ROI} and Φ_{rxn}^{211} makes clear that both reconnection-flux profiles have a gradual linear

increase preceding the largest increase in reconnection rate, which occurs at $t_{sim} \approx 176$ hr and $t_{obs} \approx 2015$ July 10 at 16:00 UT, respectively. The slope during the linear increase is greater in the observations, whereas the ARMS eruption has a more typically characteristic "impulsive" phase than is readily identifiable in the observations. We note that the duration before reaching the maximum reconnection flux is approximately 17 hr in both cases. Despite the quantitative differences in the reconnection profiles, there is a substantial qualitative agreement between the simulation results and the observational estimate of the regions on the disk face associated with the reconnection flux.

Using the Kazachenko et al. (2017) power-law scaling relation between total unsigned reconnection flux and flare strength/classification from X-ray emission, our simulation Φ_{rxn} corresponds to an unsigned flux of 1.48×10^{22} Mx and an X1.1 class flare, while the observational estimates from 211 Å correspond to 3.95×10^{21} Mx and an M1.6 class flare. The observed 1–8 Å GOES X-ray flux, however, never exceeded C1.9 between 2015 July 9–11.[7] The NOAA flare most relevant to our high-latitude filament eruption was a B7.3 flare on 2015 July 10, peaking at 01:26UT, from AR 12384 when it was positioned at S22E54. All three of the C-class flares during this period were from regions in the northern hemisphere. The lack of observed X-ray emission is consistent with the Lynch et al. (2016b) interpretation for a similarly large CME source region, whose spatial and temporal scales were of order $R_\odot$ and 24 hr, respectively. The Poynting flux associated with the reconnection flux swept into the flare current sheet provides an upper limit on the free magnetic energy available for conversion into bulk plasma heating over the flare-arcade volume. This energy is spread over such a large area at such a slow rate in this event that the resulting energy flux into the newly formed flare-arcade loops is insufficient to generate significant plasma heating and attendant X-ray emission.

It is also instructive to compare our results to the magnetic-flux estimates for other large quiet-Sun filament and/or polar-crown prominence eruptions because properties of the magnetic field (handedness, orientation, and magnetic flux content) are important quantities for making the CME–ICME connection (e.g., Démoulin 2008; Palmerio et al. 2017; Gopalswamy et al. 2018). In general, comparisons between reconnection flux and magnetic-cloud (MC) poloidal/twist flux Φ_p^{MC} measured in situ have shown robust correlations with $\Phi_{rxn} \gtrsim \Phi_p^{MC}$ (e.g., Qiu et al. 2007; Kazachenko et al. 2012; Hu et al. 2014; Gopalswamy et al. 2017). Recently, Cliver et al. (2019) calculated the reconnection flux during a large, quiet-Sun filament eruption on disk, obtaining 3.2×10^{21} Mx, very similar to our observational estimate here. Reconnection fluxes of this order of magnitude, a few times 10^{21} Mx, are comfortably within the distribution of both SDO/AIA flare reconnection fluxes (10^{20}–10^{22} Mx; Kazachenko et al. 2017) and in situ MC ICME poloidal/twist flux estimates (10^{21}–10^{22} Mx; Lynch 2005).

4.3. White-light Morphology, CME Structure, and Kinematics

To compare the simulation results with the coronagraph observations of the CME's evolution (Section 2.2), we constructed synthetic white-light images for the entire filament-activation and CME-eruption phase. The procedure was outlined in Section 3.2.
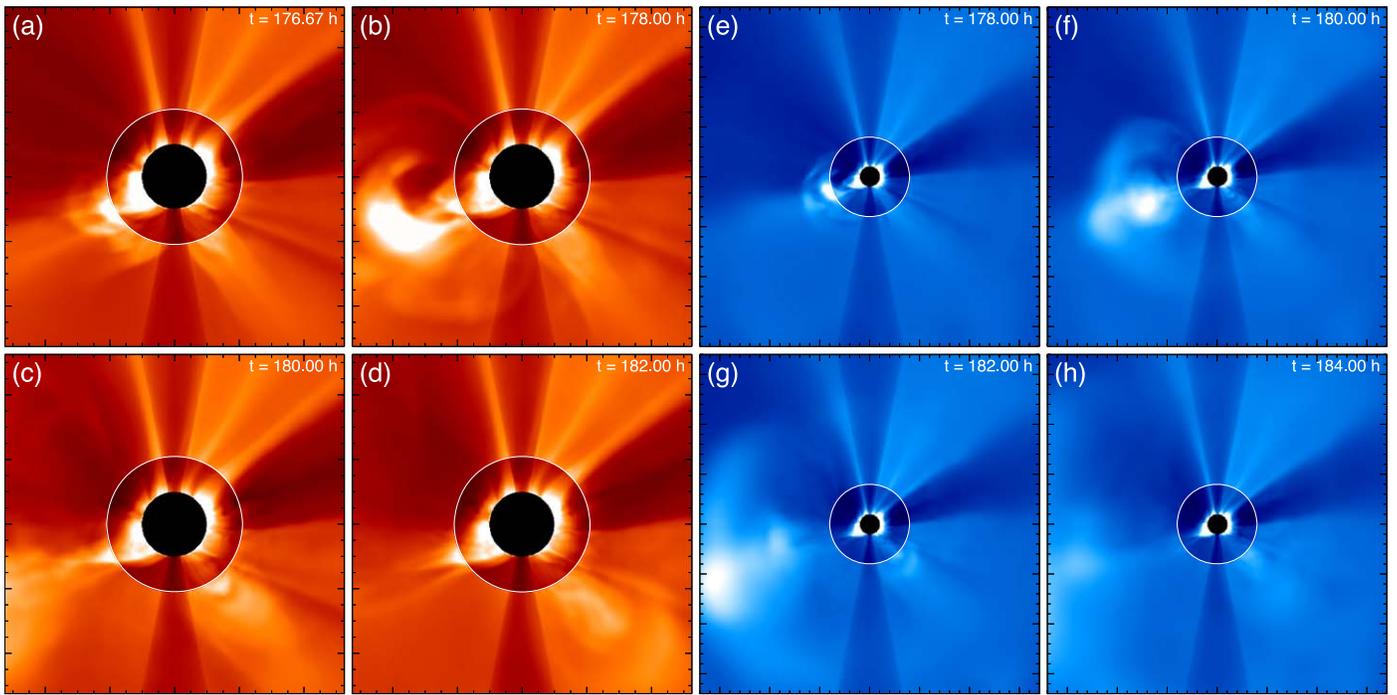

Figure 10. Synthetic white-light coronagraph images during the multistage eruption in the style of Figure 2. (a)–(d) Simulated LASCO/C2 field of view. (e)–(h) Simulated LASCO/C3 field of view. The animated version of this figure runs from $t = 160$ hr to $t = 191$ hr and shows the whole passage of the CME through the fields of view of both synthetic coronagraphs.

(An animation of this figure is available.)

Figures 10(a)–(d) show the resulting C2-like field of view ($\pm 5.25 R_\odot$ in x, y) for comparison with Figures 2(a)–(d); Figures 10(e)–(h) show the C3-like field of view ($\pm 17 R_\odot$ in x, y) for comparison with Figures 2(e)–(h). In each of the panels, we indicate the position of the C2 and C3 occulting disks at 2.1 $R_\odot$ and 4 $R_\odot$, respectively. An animated version of this figure is available.

The main features of the simulation's white-light imagery are the following. The east- and west-limb portions of the extended CME eruption are separated enough in space and time that they could easily be interpreted as two separate events. This is exactly how they are described in the CDAW LASCO CME Catalog.[8] The east-limb component of the CME features the classic "three-part" structure (e.g., Illing & Hundhausen 1985; Vourlidas et al. 2013) consisting of an enhanced leading edge, dark cavity, and bright core (see Figures 2(a), (e)). The west-limb component looks more like a classic "loop" CME without a discernible core (see Figures 2(d), (h)). Because the western portion erupts in front of a background streamer (in both observations and simulation), one might surmise that there could be an ejecta-related "core" enhancement. However, the animations of Figures 2 and 10 make clear that this is not the case.

The comparison between the white-light coronagraph imagery and the actual magnetic-field structure of the CME ejecta can be done with the simulation results in a way that is simply not possible with the observational data. Fortunately, insights obtained from examining the relationship between features of the simulation's magnetic field and synthetic white-light morphology

can be applied to the interpretation of the observational data, as well.

The animation of Figure 7(a) shows that the formation of the CME flux rope and its trajectory in the low corona are southward, but not nearly as southward as the filament-channel PIL ($-40°$ latitude), due to the rapid expansion of the CME cross-section. A part of the CME flux rope intersects the ecliptic plane for almost the entirety of the eruption. Figure 11 shows the magnetic-field evolution in our system from the "Earth viewpoint" of the synthetic coronagraph data and observations corresponding to 2015 July 10. Figures 11(a)–(d) are snapshots at exactly the same simulation times as the synthetic C3 panels in Figures 10(e)–(h). From this vantage point, we see the complex, twisted field structure of the initial east-limb part of the eruption, how much of the structure is actually Earth directed, and how the magnetic fields of the western leg of the CME open up (from east to west) toward the observer, giving rise to the flux-rope-like white-light signature on the west limb.

Quantitative comparisons between the simulated and observational data can be made with the eruption's height–time evolution and the resulting velocity profiles. We fit both the simulation and observational height/time data with the Sheeley et al. (1999) function:

$$ h(t) = r_0 + 2r_a \ln\left[\cosh\left[\frac{v_a(t + t_0)}{2r_a}\right]\right]. \quad (5) $$

This height–time expression has four free parameters that describe the initial position (r_0, t_0), the asymptotic velocity (v_a), and the length scale (r_a) over which $v(r)$ reaches 80% of v_a. The

---

[8] Available at https://cdaw.gsfc.nasa.gov/CME_list/. See entries 2015/07/09 19:00:05 (position angle 145°, width 145°) and 2015/07/10 02:24:04 (position angle 181°, width 138°).
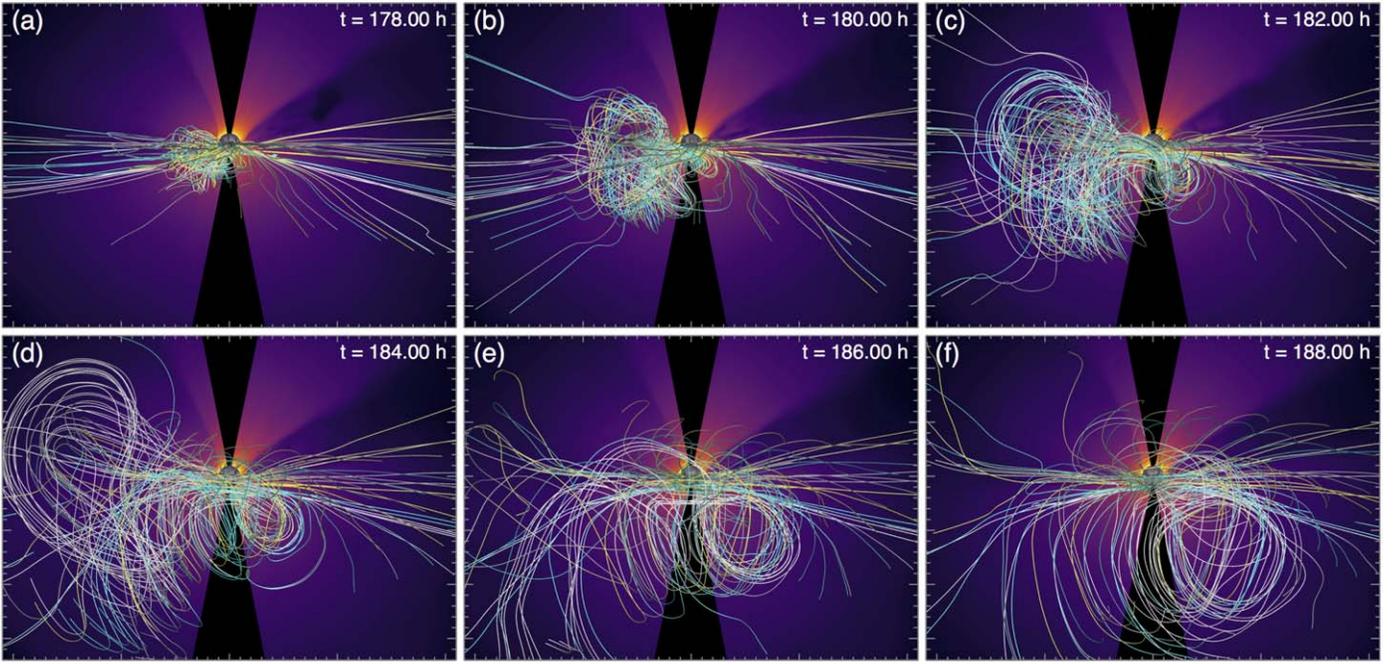
Figure 11. Representative field lines illustrating the CME's 3D magnetic structure. The log-scale mass density is shown in the plane of the sky and the image perspective is from Earth's view. Panels (a)–(d) are the same simulation times shown of the synthetic LASCO/C3 panels in Figures 10(e)–(h). The animated version of this figure runs from $t = 160$ hr to $t = 200$ hr and shows the full development of the magnetic field lines during the eruption process.

(An animation of this figure is available.)
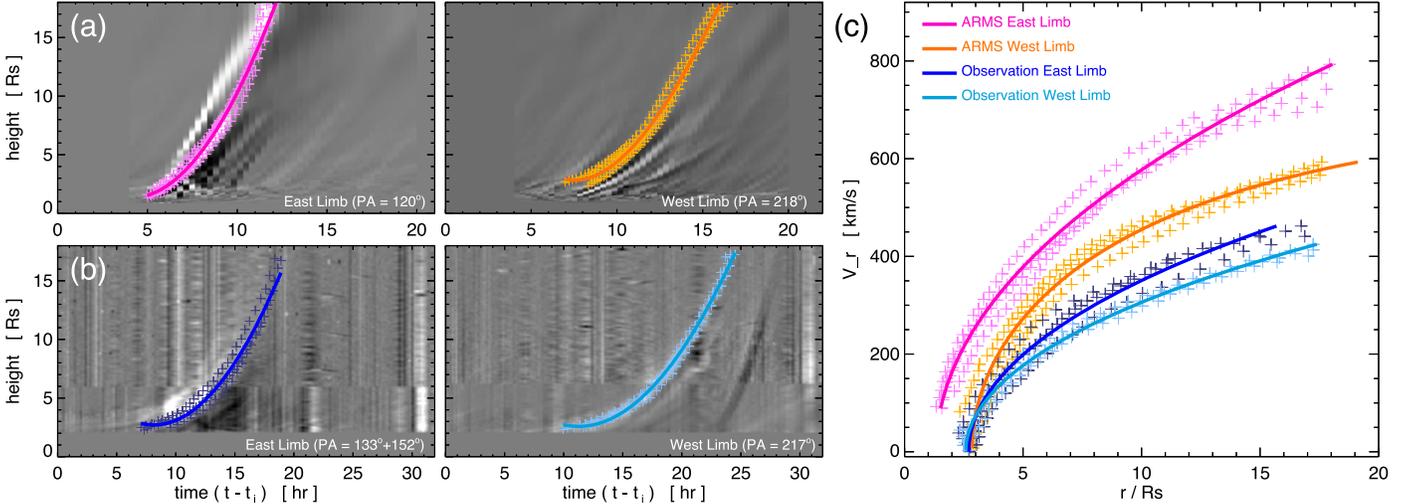
Figure 12. Height–time J-maps and functional fits to the east- and west-limb parts of the global-scale CME eruption. (a) MHD simulation results from running-difference processing of the Figure 10 animation data. (b) Observational results from running-difference processing of the Figure 2 animation data. (c) Analytic $v(r)$ profiles derived from the height–time fits.

velocity profiles are then given as

$$v(r) = v_a \left(1 - \exp \left[\frac{-(r - r_0)}{r_a} \right] \right)^{1/2}. \quad (6)$$

We used the IDL `curvefit` function to minimize the weighted χ^2 error between the parameterized $h_{\text{fit}}(t)$ expression and the height–time data,

$$\chi^2 = \frac{1}{(N-4)} \sum_{i=0}^{N} w_i (h_{\text{fit}}(t_i) - h(t_i))^2, \quad (7)$$

where the weights are simply $w_i = h^{-1}(t_i) / \max[h^{-1}(t_i)]$ and $N - 4$ is the number of data points in each profile minus the four free parameters. Figure 12(a) shows the the simulation height/time curves from the eastern limb at position angle (PA) of 120° and the western limb at PA = 218° as the magenta and orange "+" symbols. The observational height–time curves for the LASCO data are shown in Figure 12(b) as the blue and cyan "+" symbols. We constructed the eastern limb LASCO height–time data as the sum of two PAs because of the location of the LASCO/C3 occulter arm: PAs 133° and 152° are on either side of the arm and capture the leading edge of the CME; see Figures 2(e)–(h). The best-fit parameters for each of the

Table 1
Best-fit Parameters for Equations (5) and (6) for the Simulated and Observed Height/Time Coronagraph Data in Figure 12

Height/time profile	t_0	r_0	r_a	v_a	χ^2	$v_{\mathrm{fit}}(20R_\odot)$
ARMS East limb	−175.1	1.32	190.4	2733.8	0.077	835.8
ARMS West limb	−178.5	2.84	13.4	707.4	0.115	601.0
LASCO C2/C3 East limb	−24.2	2.71	110.1	1385.1	0.164	528.1
LASCO C2/C3 West limb	−27.3	2.58	102.9	1160.1	0.051	457.8

Note. The units of t_0 are hr, r_0 and r_a are $R_\odot$, and v_a and $v_{\mathrm{fit}}(20R_\odot)$ are km s^{-1}.

profiles are given in Table 1. The $v_{\mathrm{fit}}(r)$ curves are shown in Figure 12(c) in the same color scheme as the $h_{\mathrm{fit}}(t)$ profiles in Figures 12(a) and (b). The last column of Table 1 lists the v_{fit} values extrapolated to $r = 20\,R_\odot$ for each profile.

The east-limb velocity profiles in both the simulation and observations are faster than their corresponding west-limb counterparts. This agreement suggests that, although the overall energy release in our model system is larger than that inferred from the 2015 July 9–10 observations, we can use the simulation results to infer the morphological evolution of the magnetic-field structure in the event. Specifically, we can interpret the evolution of the white-light structure in the coronagraph data as corresponding to the initial east-limb component of the CME generated during the impulsive phase of the eruption that shows a higher velocity, followed by the west-limb component that presents as the leg of the extended CME flux rope opening up toward the observer with a lower velocity.

5. Discussion and Conclusions

The simulation results presented in this paper represent the first detailed calculation of a CME eruption (on 2015 July 9–10) from an extended, high-latitude PIL source region similar to the large filament-channel configurations examined by Pevtsov et al. (2012). The studied PIL and eruption extended all the way from the east to the west limb as seen from Earth. Anderson et al. (2005) have discussed the formation mechanisms of these huge filament channels. More recently, Patsourakos et al. (2020) have reviewed the magnetic structure of energized, pre-eruption states and concluded that there is likely a smooth distribution between more "sheared-arcade-like" and more "flux-rope-like" pre-eruptive configurations. The transition between the two may be an intrinsic aspect of CME initiation processes. A number of researchers have modeled the magnetic structure of these large, polar-crown filament channels (and their associated coronal cavities) using the flux-rope insertion method (van Ballegooijen 2004). For example, Su & van Ballegooijen (2012), Su et al. (2015), and Jibben et al. (2016) have all determined best-fit model twist fluxes per unit length that range from zero to a few times $10^{10}\,\mathrm{Mx\,cm}^{-1}$. Given the filament-channel lengths of 45°–120° longitude, typical poloidal/twist flux estimates are on the order of 10^{20}–$10^{21}\,\mathrm{Mx}$. Figure 7 shows that our model filament channel is clearly more of a "sheared-arcade-like" configuration, but the reconnection fluxes in both our simulation and the SDO observations result in poloidal/twist flux values entirely consistent with those earlier estimates.

One of the first comprehensive Sun-to-heliosphere analyses of a particularly strong "problem geomagnetic storm" was the 1994 April 14 event discussed by McAllister et al. (1996). The on-disk signatures for that extended filament-channel eruption included Yohkoh soft X-ray observations of a massive PEA that formed over the course of ∼10 hr to span ∼150° in longitude and 30°–40° in latitude on the disk face. Ground-based coronagraph observations from K-Cor were able to resolve the helmet-streamer belt in the southern hemisphere overlying the extended PIL with indications of a streamer-blowout on the southeastern limb. McAllister et al. (1996, p. 13502) conclude, "Thus, although there was no direct observation of a white-light CME on April 14, the existing data strongly support the conclusion that a CME did in fact take place."

Zhukov & Veselovsky (2007) have examined global-scale dimming signatures associated with X-class flares and their resulting halo CMEs. Their classification of a "global" eruption was based on EUV dimmings on the limb that were $\gtrsim 180°$ in angular extent. There are a number of examples of sympathetic eruptions, where a CME triggers subsequent eruptions (e.g., Török et al. 2011; Schrijver et al. 2013), and this scenario may explain global EUV dimming observations, at least in some cases. In the event modeled here, both the observations and simulation present EUV signatures suggesting that an eruption occurred across a comparably sized source region. However, there was no obvious off-limb dimming signature nor were the SDO/AIA 211 Å dimmings especially dramatic, despite the event being a clearly "global" eruption.

Forward-modeling of synthetic white-light images using the simulation's mass-density data enabled us to interpret the coronagraph observations during this event in a particularly illuminating way. Specifically, the seemingly disparate CME events from opposite limbs, listed as two separate CMEs occurring over 7 hr apart in the LASCO CME catalog, have been shown here to be consistent with a single, gradual eruption from a high-latitude PIL. The 2015 July 9–10 large-scale filament eruption can be considered an asymmetric eruption of the type discussed by, e.g., Tripathi et al. (2006) and Liu et al. (2009). In both the observations and our simulation, the east-limb magnetic fields erupt first, and the eruption thereafter proceeds to sweep from east to west along the PIL.

McCauley et al. (2015) created a catalog of SDO prominence and filament eruptions and examined the statistics for events organized by various properties and source-region types (i.e., active region, intermediate, quiescent, and polar crown). For example, symmetric filament eruptions are slightly more common (48%) than asymmetric eruptions (38%) over the whole data set and in each source-region type, with the exception of polar-crown filaments whose eruptions were 39% symmetric and 45% asymmetric. McCauley et al. (2015) suggested that the longer filaments may provide more opportunity for localized destabilization, which then propagates along the energized filament channel—in excellent qualitative agreement with our simulation results.

Polar-crown and quiet-Sun erupting filaments are known to deflect away from coronal holes and toward the equator and/or the streamer belt and HCS (e.g., Kilpua et al. 2009; Panasenco et al. 2013). In the McCauley et al. (2015) survey, approximately 25% of filament eruptions propagate nonradially or exhibit an even more extreme deflection (e.g., erupting sideways). Gopalswamy et al. (2015) showed that deflections up to ~30° in the LASCO coronagraph field of view are fairly common for polar-crown filament CMEs. The 2015 July 9–10 CME does not appear to have a significant deflection during the eruption in either observations or our simulation. In part, this is because the filament channel is comfortably under a high-latitude excursion of the helmet-streamer belt. Thus, our eruption is more of a classic streamer-blowout CME (Lynch et al. 2016b; Vourlidas & Webb 2018) that happens to originate from the helmet-streamer belt at −40° latitude.

However, despite the high-latitude source region, the rapidly expanding CME eruption becomes large enough to intersect the equatorial plane. This includes the top of the coherent, magnetic flux-rope ejecta, which is easily seen in the simulation magnetic-field evolution (Figures 7 and 11), but neither the observed or synthetic coronagraph imagery show an obvious component of the CME in the ecliptic headed toward Earth. While the initial east-limb white-light structure of our model eruption is larger and more equatorial than the observations, the west-limb part of the simulation CME is in much better agreement with the apparent propagation direction (see Figures 2 and 10).

The intersection with the ecliptic plane is important because this high-latitude filament-eruption CME impacted Earth. The ICME was observed by the Wind and ACE spacecraft beginning on 2015 July 13, and the in situ magnetic-field and plasma measurements exhibit various properties compatible with typical magnetic-cloud/flux-rope signatures. Additionally, this particular ICME had a sustained period of southward B_z, which caused a moderate geomagnetic disturbance (peak minimum Dst of −61 nT). Both the impact and the geoeffectiveness of this event may have been unexpected, given the seemingly disparate eruptions in the LASCO data that were both slow and apparently directed more southward than toward Earth.

The original definition of a "stealth CME" is an event that lacks clear, on-disk eruption signatures but can be visible in coronagraph observations, especially away from the Sun–Earth line. The opposite scenario also happens: There can be eruption signatures on the disk but no readily identifiable or significant CME counterpart in coronagraph data. The 2015 July 9–10 event and our simulation fall into a third, much more general category: ambiguous on-disk eruption signatures with ambiguous coronagraph signatures. Here, the "stealthiness" is not missing observational signatures; rather, it represents the uncertainty in assessing the likelihood of an Earth impact and/or its geoeffectiveness (i.e., what makes a problem geomagnetic storm "problematic"). In a future paper, we intend to analyze the interplanetary propagation of this high-latitude filament-channel eruption; examine its in situ plasma, field, and composition characteristics; and model its Sun-to-Earth evolution.

Appendix A
STITCH Energization Parameters

The STITCH formalism represents the introduction of horizontal magnetic flux at the lower boundary, allowing for the accumulation of a nonpotential shear/twist component of the magnetic field concentrated above our large-scale polarity inversion line. The details and justification of the physical basis for the statistically averaged helicity condensation model and its implementation for modeling the long-term, nonpotential evolution of the global solar corona can be found in the appendix of Mackay et al. (2014).

In ARMS, the STITCH contribution is implemented as a source term in the induction equation, contributing new horizontal components of the magnetic field, $\partial \boldsymbol{B}_S/\partial t$, given by Equation (1). The B_θ, B_ϕ components of the magnetic field are defined at their respective cell faces. The STITCH updates are

<div style="text-align:center">

Table 2
Parameters for the Spatial and Temporal Dependence of $\zeta^{(i)}(\theta, \phi, t)$

</div>

		$f_\theta(\theta)$				$f_\phi(\phi)$				$f_t(t)$				$f_B(B_r)$
i	K_0[a]	k_θ	θ_l (°)	θ_r (°)	θ_c (°)	k_ϕ	ϕ_l (°)	ϕ_r (°)	ϕ_c (°)	k_t	t_l (hr)	t_r (hr)	t_c (hr)	P_B
1	1.0 (0.50)	1.0	−55	−10	−10	0.5	0	120	0	1.0	100 (160)	130 (180)	100 (160)	+1
2	−1.5 (−0.75)	1.0	−65	−20	−20	0.5	0	120	0	1.0	100 (160)	130 (180)	100 (160)	−1
3	1.0 (0.50)	1.0	−55	−20	−20	2.0	20	120	20	1.0	100 (160)	130 (180)	100 (160)	+1
4	−1.0 (−0.50)	1.0	−65	−20	−20	2.0	20	120	20	1.0	100 (160)	130 (180)	100 (160)	−1
5	1.5 (0.75)	1.0	−45	−20	−20	1.0	95	120	95	1.0	100 (160)	130 (180)	100 (160)	+1
6	−1.5 (−0.75)	1.0	−45	−20	−20	1.0	95	120	95	1.0	100 (160)	130 (180)	100 (160)	−1
7	1.5 (0.75)	1.0	−51	−23	−23	1.0	20	120	20	1.0	100 (160)	130 (180)	100 (160)	+1
8	−1.5 (−0.75)	1.0	−65	−25	−25	1.0	20	120	20	1.0	100 (160)	130 (180)	100 (160)	−1

Note.
[a] Units of the scalar coefficient are 10^{15} cm^2 s^{-1}.

applied to the bottom-most computational grid cells in the domain and are then transported farther upward into the domain by convection. The radial component, B_r, on the inner radial boundary (half a grid cell below the B_θ, B_ϕ components) remains unchanged by the STITCH energization. The STITCH contributions are calculated from the curl of a set of functions $\zeta^{(i)} B_r(\theta, \phi) \hat{r}$. The form of $\zeta^{(i)}$ is given in Equation (2) as the product of spatial and temporal envelope functions $f_\theta(\theta), f_\phi(\phi)$, and $f_t(t)$ applied to regions of positive or negative magnetic polarity via $f_B(B_r)$. The θ and ϕ envelope functions are given by

$$f_\theta(\theta) = \frac{1}{2} - \frac{1}{2}\cos\left[2\pi k_\theta \frac{(\theta - \theta_c)}{(\theta_r - \theta_l)}\right], \qquad (A1)$$

$$f_\phi(\phi) = \begin{cases} \sin\left[2\pi k_\phi \dfrac{(\phi - \phi_c)}{(\phi_r - \phi_l)}\right] & \text{for } i = 1, 2 \\[2mm] \dfrac{1}{2} - \dfrac{1}{2}\cos\left[2\pi k_\phi \dfrac{(\phi - \phi_c)}{(\phi_r - \phi_l)}\right] & \text{for } i \geqslant 3 \end{cases}, \quad (A2)$$

and the temporal dependence is given by

$$f_t(t) = \frac{1}{2} - \frac{1}{2}\cos\left[2\pi k_t \frac{(t - t_c)}{(t_r - t_l)}\right]. \qquad (A3)$$

The l, r, and c subscripts just refer to the left, right, and centering values that define the spatial or temporal range of the θ, ϕ, and t envelope functions. The masking of the B_r polarities is specified by

$$f_B(B_r) = \begin{cases} 1 & \text{for } B_r/|B_r| = P_B \\ 0 & \text{elsewhere} \end{cases}. \qquad (A4)$$

We use $N = 8$ separate $\zeta^{(i)}(B_r, \theta, \phi, t)$ patterns that are added together to generate the final helicity-injection distribution. Each of the parameter sets for the spatial and temporal functions are given in Table 2. As described in Sections 3.3 and 4.1, we performed two phases of helicity injection and magnetic-field energization with this pattern: the first for $100\,\text{hr} \leqslant t \leqslant 130\,\text{hr}$, and the second for $160\,\text{hr} \leqslant t \leqslant 180\,\text{hr}$. The parameters used in the second phase, "Activation and Eruption," are listed in parentheses where they differ from the parameters of the first phase, "Filament-channel Energization." Figure 13(a) shows the resulting $\sum \zeta^{(i)} B_r$ distribution at its maximum during the filament-channel energization phase, when $f_t(115\,\text{hr}) = 1.0$. The magnitudes of the four STITCH patterns acting on the positive-polarity regions ($i = 1, 3, 5, 7$)
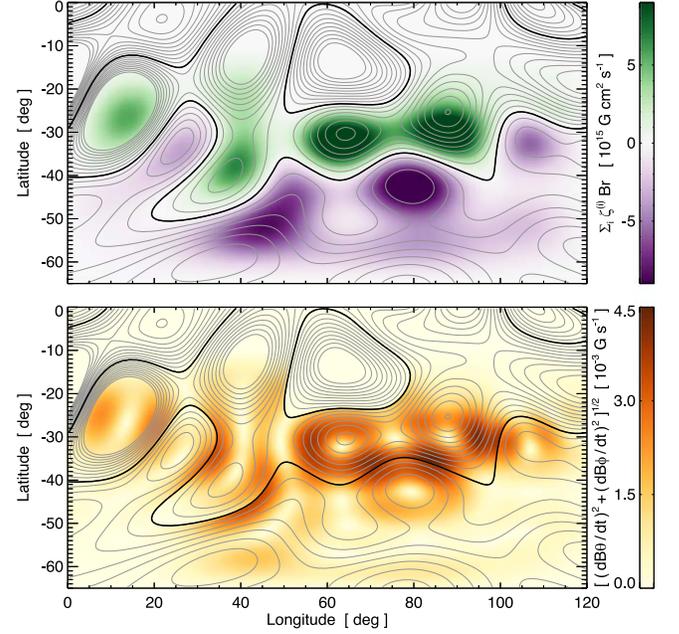

Figure 13. The top panel shows the summation of the eight different $\zeta^{(i)} B_r$ contributions used to construct the STITCH energization boundary conditions. The bottom panel shows the magnitude of the STITCH horizontal field changes $[(\partial B_\theta/\partial t)^2 + (\partial B_\phi/\partial t)^2]^{1/2}$.

are shown in green, while the negative-polarity patterns ($i = 2, 4, 6, 8$) are shown in purple. Figure 13(b) shows the magnitude of the right-hand side of Equation (1) in units of 10^{-3} G s^{-1}. The magnitude pattern for $50° \leqslant \phi \leqslant 120°$ shows a series of rings that reflect the $\zeta^{(i)} B_r$ component patterns defined above. The individual $\partial B_\theta/\partial t$ and $\partial B_\phi/\partial t$ components that make up the Figure 13(b) helicity-injection magnitude are shown in Figure 5. These components, when plotted separately, illustrate the cumulative effect of multiple helicity-injection patterns, creating a coherent, sheared-field filament channel above the complex, high-latitude PIL.

Appendix B
AIA Flare Ribbon/Post-eruption Arcade Pixel Masks

The identification and tracking of flare ribbons is often done with 1600 Å UV emission data (e.g., Qiu 2009). Kazachenko et al. (2017) developed an empirical thresholding technique to compensate for CCD saturation and pixel blooming, in order to smoothly accumulate the total area swept out by the flare-
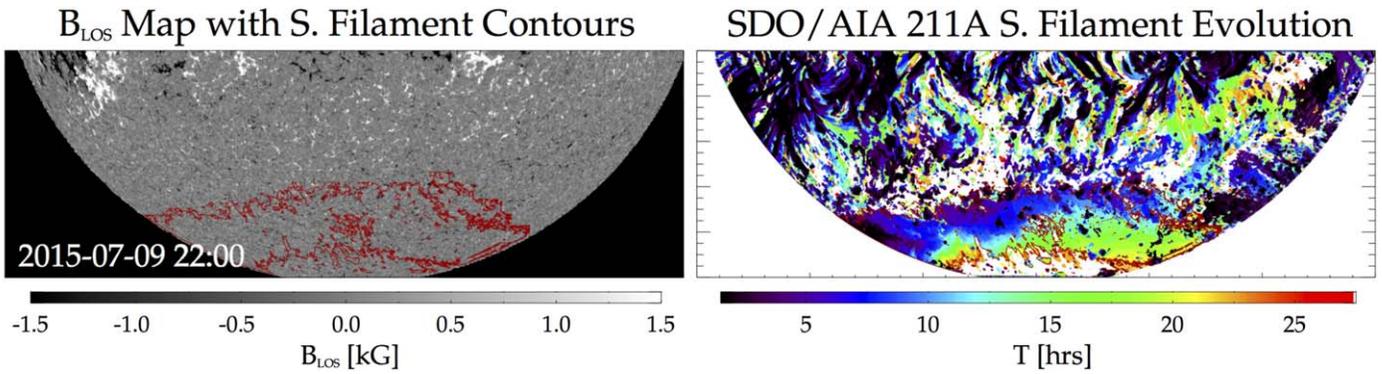
<div style="text-align:center">15</div>

B$_{\mathrm{LOS}}$ Map with S. Filament Contours

2015-07-09 22:00

-1.5   -1.0   -0.5   0.0   0.5   1.0   1.5
B$_{\mathrm{LOS}}$ [kG]

SDO/AIA 211A S. Filament Evolution

5   10   15   20   25
T [hrs]

Figure 14. The left panel shows the post-eruption arcade area (red contour) used to estimate the negative-polarity reconnection flux $\Phi^{211}_{\mathrm{rxn}}$ from the HMI B_{LOS} data. The right panel shows the cumulative ribbon area, with each pixel colored according to the first time the reconnection threshold was exceeded in the running-difference AIA 211 Å image.

ribbon motions. As discussed in Section 2.1, however, the 2015 July 9–10 filament eruption does not generate these traditional flare-ribbon emission signatures. On the other hand, Figure 1 and its animation show EUV signatures that are suggestive of ribbon-like evolution but are more clearly indicative of the post-eruption arcade (PEA) brightening and the refilling of eruption-related EUV dimmings. We note that the area underneath the PEA can be used to estimate the reconnection flux (see, e.g., Gopalswamy et al. 2017), but this technique is typically used at a single time corresponding to the maximum area of the PEA emission.

We used a 48 hr sequence of AIA images in the 211 Å channel, from 2015 July 9 at 16:00 UT until 2015 July 11 at 15:30 UT with a 30 minute temporal cadence and a $0''\!.6$ pixel size to track the evolution of the PEA boundaries. Because the evolution was not well seen in individual images, we used difference images 30 minutes apart to track the boundary motions. We smoothed each difference image with a 10×10 pixel boxcar average and identified pixels where the intensity was greater than three exposure-normalized data counts in the difference image to construct the cumulative pixel mask array $M_{i,j}$. We then rotated the derived filament mask sequence using `diff_rot.pro` in SolarSoft to the first image when the filament started rising (2015 July 9 at 23:00 UT) to compensate for the solar rotation.

Figure 14 shows the evolution of the identified southern portion of the PEA. Panel (a) shows the HMI line-of-sight (LOS) field B_{LOS} with the cumulative ribbon mask area denoted by the red contours. Panel (b) shows the time at which each individual pixel met the running-difference intensity threshold. We were not able to track the flare-arcade area north of the PIL unambiguously, due to the presence of bright emission from several large active regions. We calculated the evolution of the total reconnection flux associated with the southern half of the filament channel from the cumulative ribbon mask $M^{211}_{i,j}$ corresponding to the negative-polarity region ($B_r \leqslant 0$) as

$$\Phi^{211}_{\mathrm{rxn}} = \int |B^{(-)}_r| \, dA^{211}$$
$$= \sum_{i,j} \frac{|B^{(-)}_{\mathrm{LOS}}|}{\cos^2 \theta} \, M^{211}_{i,j} \, dA_{i,j}. \qquad (B1)$$

In the magnetic flux calculation, we only considered magnetic fields above the noise level $B_{\mathrm{LOS}} = 15$ G. The $\cos^2 \theta$ factor comes from deprojecting the LOS magnetic fields

onto the radial direction $B^{(-)}_r = B^{(-)}_{\mathrm{LOS}} / \cos \theta$ and taking into account the foreshortening of the surface area in each pixel ($dA^{211} = dA_{i,j} / \cos \theta$). Figure 14(b) shows the classic time-integrated two-ribbon-flare evolution signatures (Qiu 2009; Aulanier et al. 2012; Kazachenko et al. 2017), but for just the southern ribbon. This reconnection-flux area quickly extends from east to west during $5 \, \mathrm{hr} \lesssim t \lesssim 10 \, \mathrm{hr}$, corresponding to rapid growth parallel to the global PIL. Afterwards, the southern half of the PEA area grows more slowly during $10 \, \mathrm{hr} \lesssim t \lesssim 25 \, \mathrm{hr}$, perpendicular to the global PIL. Our reconnection flux estimate during the filament eruption is shown in Figure 9(b) as the black line with square symbols. The reconnection rate is defined as $d\Phi^{211}_{\mathrm{rxn}}/dt$, calculated using the standard central-difference formula. Our reconnection rate estimate is shown in Figure 9(b) as the purple line.

ORCID iDs

Benjamin J. Lynch https://orcid.org/0000-0001-6886-855X
Erika Palmerio https://orcid.org/0000-0001-6590-3479
C. Richard DeVore https://orcid.org/0000-0002-4668-591X
Maria D. Kazachenko https://orcid.org/0000-0001-8975-7605
Joel T. Dahlin https://orcid.org/0000-0002-9493-4730
Jens Pomoell https://orcid.org/0000-0003-1175-7124
Emilia K. J. Kilpua https://orcid.org/0000-0002-4489-8073

References

Anderson, M., & Martin, S. F. 2005, in ASP Conf. Ser. 346 Large-scale Structures and their Role in Solar Activity, ed. K. Sankarasubramanian, M. Penn, & A. Pevtsov (San Francisco, CA: ASP), 201
Antiochos, S. K. 2013, ApJ, 772, 72
Aulanier, G., Janvier, M., & Schmieder, B. 2012, A&A, 543, A110
Billings, D. E. 1966, A Guide to the Solar Corona (New York: Academic)
Brueckner, G. E., Howard, R. A., Koomen, M. J., et al. 1995, SoPh, 162, 357
Chae, J., Cho, K., Kwon, R.-Y., & Lim, E.-K. 2017, ApJ, 841, 49
Cliver, E. W., Kahler, S. W., Kazachenko, M., & Shimojo, M. 2019, ApJ, 877, 11
Dahlin, J. T., Antiochos, S. K., & DeVore, C. R. 2019a, ApJ, 879, 96
Dahlin, J. T., Antiochos, S. K., & DeVore, C. R. 2019b, AAS Meeting, 51, 317.03
Démoulin, P. 2008, AnGeo, 26, 3113
DeVore, C. R. 1991, JCoPh, 92, 142
DeVore, C. R., & Antiochos, S. K. 2000, ApJ, 539, 954
DeVore, C. R., & Antiochos, S. K. 2008, ApJ, 680, 740
Domingo, V., Fleck, B., & Poland, A. I. 1995, SoPh, 162, 1
Forbes, T. G., & Priest, E. R. 1983, SoPh, 84, 169
Freeland, S. L., & Handy, B. N. 1998, SoPh, 182, 497
Gibson, S. E. 2018, LRSP, 15, 7

Gopalswamy, N., Akiyama, S., Yashiro, S., & Xie, H. 2018, in Space Weather of the Heliosphere: Processes and Forecasts, ed. C. Foullon & O. E. Malandraki, Vol. 335 (Cambridge: Cambridge Univ. Press), 258
Gopalswamy, N., Yashiro, S., Akiyama, S., & Xie, H. 2017, SoPh, 292, 65
Gopalswamy, N. 2015, in Solar Prominences, ed. J.-C. Vial & O. Engvold, Vol. 415 (Cham: Springer), 381
Harvey, J. W., Hill, F., Hubbard, R. P., et al. 1996, Sci, 272, 1284
Hu, Q., Qiu, J., Dasgupta, B., Khare, A., & Webb, G. M. 2014, ApJ, 793, 53
Illing, R. M. E., & Hundhausen, A. J. 1985, JGR, 90, 275
Jibben, P., Reeves, K., & Su, Y. 2016, FrASS, 3, 10
Karpen, J. T., Antiochos, S. K., & DeVore, C. R. 2012, ApJ, 760, 81
Kazachenko, M. D., Canfield, R. C., Longcope, D. W., & Qiu, J. 2012, SoPh, 277, 165
Kazachenko, M. D., Lynch, B. J., Welsch, B. T., & Sun, X. 2017, ApJ, 845, 49
Kilpua, E. K. J., Pomoell, J., Vourlidas, A., et al. 2009, AnGeo, 27, 4491
Knizhnik, K. J., Antiochos, S. K., & DeVore, C. R. 2015, ApJ, 809, 137
Knizhnik, K. J., Antiochos, S. K., & DeVore, C. R. 2017a, ApJ, 835, 85
Knizhnik, K. J., Antiochos, S. K., DeVore, C. R., & Wyper, P. F. 2017b, ApJL, 851, L17
Lemen, J. R., Title, A. M., Akin, D. J., et al. 2012, SoPh, 275, 17
Linton, M. G., & Moldwin, M. B. 2009, JGR, 114, A00B09
Liu, R., Alexander, D., & Gilbert, H. R. 2009, ApJ, 691, 1079
Luhmann, J. G., Gosling, J. T., Hoeksema, J. T., & Zhao, X. 1998, JGR, 103, 6585
Lynch, B. J., Airapetian, V. S., DeVore, C. R., et al. 2019, ApJ, 880, 97
Lynch, B. J., & Edmondson, J. K. 2013, ApJ, 764, 87
Lynch, B. J., Edmondson, J. K., Kazachenko, M. D., & Guidoni, S. E. 2016a, ApJ, 826, 43
Lynch, B. J., Gruesbeck, J. R., Zurbuchen, T. H., & Antiochos, S. K. 2005, JGR, 110, A08107
Lynch, B. J., Masson, S., Li, Y., et al. 2016b, JGRA, 121, 10677
Mackay, D. H., DeVore, C. R., & Antiochos, S. K. 2014, ApJ, 784, 164
Mackay, D. H., DeVore, C. R., Antiochos, S. K., & Yeates, A. R. 2018, ApJ, 869, 62
Mackay, D. H., Karpen, J. T., Ballester, J. L., Schmieder, B., & Aulanier, G. 2010, SSRv, 151, 333
MacNeice, P., Olson, K. M., Mobarry, C., de Fainchtein, R., & Packer, C. 2000, CoPhC, 126, 330
McAllister, A. H., Dryer, M., McIntosh, P., Singer, H., & Weiss, L. 1996, JGR, 101, 13497

McCauley, P. I., Su, Y. N., Schanche, N., et al. 2015, SoPh, 290, 1703
Moore, R. L., Sterling, A. C., Hudson, H. S., & Lemen, J. R. 2001, ApJ, 552, 833
Müller, D., Nicula, B., Felix, S., et al. 2017, A&A, 606, A10
Nitta, N. V., & Mulligan, T. 2017, SoPh, 292, 125
Palmerio, E., Kilpua, E. K. J., James, A. W., et al. 2017, SoPh, 292, 39
Panasenco, O., Martin, S. F., Velli, M., & Vourlidas, A. 2013, SoPh, 287, 391
Parenti, S. 2014, LRSP, 11, 1
Parker, E. N. 1958, ApJ, 128, 664
Patsourakos, S., Vourlidas, A., Török, T., et al. 2020, SSRv, 216, 131
Pesnell, W. D., Thompson, B. J., & Chamberlin, P. C. 2012, SoPh, 275, 3
Pevtsov, A. A., Berger, M. A., Nindos, A., Norton, A. A., & van Driel-Gesztelyi, L. 2014, SSRv, 186, 285
Pevtsov, A. A., Panasenco, O., & Martin, S. F. 2012, SoPh, 277, 185
Priest, E. R., & Longcope, D. W. 2017, SoPh, 292, 25
Qiu, J. 2009, ApJ, 692, 1110
Qiu, J., Hu, Q., Howard, T. A., & Yurchyshyn, V. B. 2007, ApJ, 659, 758
Riley, P., Lionello, R., Mikić, Z., et al. 2007, ApJ, 655, 591
Robbrecht, E., Patsourakos, S., & Vourlidas, A. 2009, ApJ, 701, 283
Scherrer, P. H., Schou, J., Bush, R. I., et al. 2012, SoPh, 275, 207
Schrijver, C. J., Title, A. M., Yeates, A. R., & DeRosa, M. L. 2013, ApJ, 773, 93
Sheeley, N. R., Walters, J. H., Wang, Y. M., & Howard, R. A. 1999, JGR, 104, 24739
Sheeley, N. R., Jr., Wang, Y.-M., Hawley, S. H., et al. 1997, ApJ, 484, 472
Sterling, A. C., & Moore, R. L. 2003, ApJ, 599, 1418
Su, Y., & van Ballegooijen, A. 2012, ApJ, 757, 168
Su, Y., van Ballegooijen, A., McCauley, P., et al. 2015, ApJ, 807, 144
SunPy Community, Barnes, W. T., Bobra, M. G., et al. 2020, ApJ, 890, 68
Thompson, B. J., Cliver, E. W., Nitta, N., Delannée, C., & Delaboudinière, J.-P. 2000, GeoRL, 27, 1431
Török, T., Panasenco, O., Titov, V. S., et al. 2011, ApJL, 739, L63
Tripathi, D., Isobe, H., & Mason, H. E. 2006, A&A, 453, 1111
van Ballegooijen, A. A. 2004, ApJ, 612, 519
Vourlidas, A., & Howard, R. A. 2006, ApJ, 642, 1216
Vourlidas, A., Lynch, B. J., Howard, R. A., & Li, Y. 2013, SoPh, 284, 179
Vourlidas, A., & Webb, D. F. 2018, ApJ, 861, 103
Wang, Y.-M., & Sheeley, N. R., Jr. 1992, ApJ, 392, 310
Webb, D. F., & Vourlidas, A. 2016, SoPh, 291, 3725
Zhukov, A. N., & Veselovsky, I. S. 2007, ApJL, 664, L131